AD-A071 650 TRITEC INC COLUMBIA MD F/G 13/7
DEVELOPMENT OF CRITICAL FLUIDIC COMPONENTS,(U)
JUL 78 K C CHEN, V F NERADKA DAAG39-77-C-0173
UNCLASSIFIED HDL-CR-78-173-1 NL

| OF |
AD
A071650

END
DATE FILMED
8-79
DDC

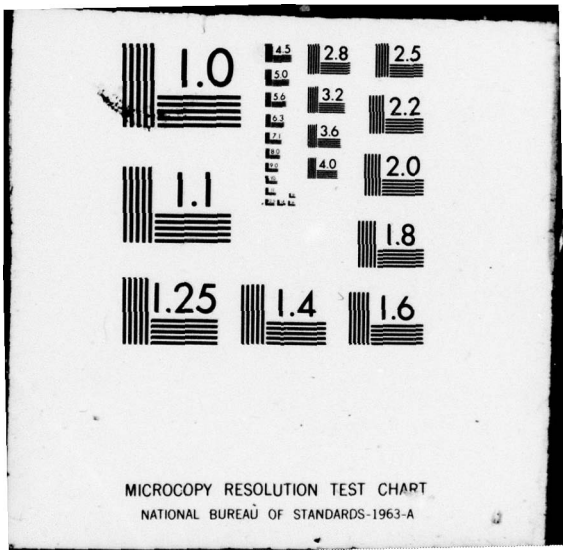
1.0
1.1
1.25
1.4
1.6
1.8
2.0
2.2
2.5
2.8
3.2
3.6
4.0
4.5
5.0
5.6
6.3
MICROCOPY RESOLUTION TEST CHART
NATIONAL BUREAU OF STANDARDS-1963-A

LEVEL II

12

B.S.

HDL-CR-78-173-1

DEVELOPMENT OF CRITICAL FLUIDIC COMPONENTS

by

Kevin C.S. Chen and Vincent F. Neradka

MARCH 1979

Prepared by

TRITEC, INC.
P.O. BOX 56
8925-11 MCGAW COURT
COLUMBIA, MARYLAND 21045

Under contract

DAAG39-77-C-0173

U.S. Army Electronics Research
and Development Command
Harry Diamond Laboratories
Adelphi, MD 20783

Approved for public release; distribution unlimited.

The findings in this report are not to be construed as an official Department of the Army position unless so designated by other authorized documents.

Citation of manufacturers' or trade names does not constitute an official endorsement or approval of the use thereof.

Destroy this report when it is no longer needed. Do not return it to the originator.

UNCLASSIFIED

SECURITY CLASSIFICATION OF THIS PAGE *(When Data Entered)*

REPORT DOCUMENTATION PAGE

READ INSTRUCTIONS BEFORE COMPLETING FORM

1. REPORT NUMBER: HDL-CR-78-173-1	2. GOVT ACCESSION NO.
3. RECIPIENT'S CATALOG NUMBER	
4. TITLE *(and Subtitle)*: Development of Critical Fluidic Components	5. TYPE OF REPORT & PERIOD COVERED: Contractor Report
	6. PERFORMING ORG. REPORT NUMBER
7. AUTHOR(s): Kevin C. S. Chen and Vincent F. Neradka	8. CONTRACT OR GRANT NUMBER(s): DAAG39-77-C-0173 New
9. PERFORMING ORGANIZATION NAME AND ADDRESS: TRITEC, INC. P.O. BOX 56, 8925-11 MC GAW CT. COLUMBIA, MD.21045	10. PROGRAM ELEMENT, PROJECT, TASK AREA & WORK UNIT NUMBERS: 6.21.14A
11. CONTROLLING OFFICE NAME AND ADDRESS: Harry Diamond Laboratories, 2800 Powder Mill Road, Adelphi, Maryland 20783	12. REPORT DATE: 14 July 1978 13. NUMBER OF PAGES: 80
14. MONITORING AGENCY NAME & ADDRESS *(if different from Controlling Office)*	15. SECURITY CLASS. *(of this report)*: UNCLASSIFIED 15a. DECLASSIFICATION/DOWNGRADING SCHEDULE

16. DISTRIBUTION STATEMENT *(of this Report)*

Approved for public release; distribution unlimited.

17. DISTRIBUTION STATEMENT *(of the abstract entered in Block 20, if different from Report)*

18. SUPPLEMENTARY NOTES

HDL Project: 304734

19. KEY WORDS *(Continue on reverse side if necessary and identify by block number)*

Fluidics, Rate Sensors, Vortex Rate Sensor, Laminar Jet Angular Rate Sensor

20. ABSTRACT *(Continue on reverse side if necessary and identify by block number)*

This report is an independent assessment of the performance of three fluidic rate sensors which were provided ~~to TRITEC~~ for test. All tests were run using MIL-H-5606 hydraulic fluid. The results of the testing showed that the Fluidisc had the lowest threshold and null sensitivity, and that its output is sufficient to directly drive some hydraulic components. On the other hand the Laminar Angular Rate Sensor is the most economical sensor and its low noise and power consumption makes it the sensor having the most potential for future applications.

DD FORM 1 JAN 73 1473 EDITION OF NOV 65 IS OBSOLETE

UNCLASSIFIED

AD 393775

FOREWORD

This document is the final report of a program to assess the performance of three fluidic rate sensors. The work was performed under Contract No. DAAG39-77-C-0173, under the technical direction of Mr. James Joyce. Special appreciation is hereby noted to Mr. James Joyce, Mr. Francis Manion, Mr. Tadeus Drzeweicki, and others of the Harry Diamond Laboratories staff who contributed their time and support in providing their sensors, documentation, and technical expertise.

TABLE OF CONTENTS

		PAGE
1.0	INTRODUCTION	7
2.0	CONCLUSIONS AND RECOMMENDATIONS	8
3.0	COMPARISON OF THE FDSC, LARS, AND VRS	10
	3.1 Sensitivity	
	3.2 Bandwidth	
	3.3 Null Shift	
	3.4 Cross-Axis Sensitivity	
	3.5 Output Impedance	
4.0	FLUIDISC RATE GYRO ANALYSIS	20
	4.1 Flapper Nozzle Considerations	
	4.2 Sensitivity	
	4.3 Bandwidth	
	4.4 Null Shift and Cross-Axis Sensitivity	
	4.5 Supply Pressure and Flow Characteristics	
	4.6 Threshold	
5.0	LAMINAR JET ANGULAR RATE SENSOR ANALYSIS	38
	5.1 Sensitivity	
	5.2 Bandwidth	
	5.3 Maximum Rate of the Sensor	
	5.4 Output Impedance	
	5.5 Threshold	
	5.6 Cross-Axis Sensitivity	
6.0	VORTEX RATE SENSOR ANALYSIS	52
	6.1 Sensitivity	
	6.2 Bandwidth	
	6.3 Output Impedance	
	6.4 Threshold	
	6.5 Null Shift	
	6.5.1 Null Shift vs Supply Pressure	
	6.5.2 Null Shift vs Temperature	
	6.6 Cross-Axis Sensitivity	
APPENDIX A:	Sensitivity Optimization Analysis of Fluidisc Bridge Circuit	60
LIST OF REFERENCES		75

LIST OF FIGURES

		PAGE
Figure 3-1.	Sensitivity vs supply pressure	12
Figure 3-2.	Null shift vs supply pressure	13
Figure 3-3.	Supply pressure vs flow rate	14
Figure 3-4.	Null shift vs temperature	16
Figure 3-5a.	Cross-axis sensitivity (Z axis)	17
Figure 3-5b.	Cross-axis sensitivity (Y axis)	18
Figure 3-6.	Cross-axes of LARS and FDSC	19
Figure 4-1.	Analogy between hydraulic rate gyro and conventional electromechnaical rate gyro	20
Figure 4-2	Flapper nozzle general arrangement	21
Figure 4-3.	Block diagram of FDSC	21
Figure 4-4.	Block diagram for finite impedance load	22
Figure 4-5.	FDSC block diagram reduction	23
Figure 4-6.	Flapper nozzle	24
Figure 4-7.	Flat-flaced flapper nozzle	24
Figure 4-8.	FDSC output vs applied rate	26
Figure 4-9.	FDSC scale factor vs supply pressure	27
Figure 4-10.	Schematic of FDSC flow path	28
Figure 4-11.	Variation of flapper output pressure with gap	28
Figure 4-12.	Dimensions of the aluminum boundaries to the spiral flow passageways.	29
Figure 4-13.	FDSC frequency response plot	30
Figure 4-14.	FDSC block diagram with torquing nozzles	31
Figure 4-14a.	"Output axis" cross-axis sensitivity	32
Figure 4-14b.	"Angular momentum" cross-axis sensitivity for two test runs	33
Figure 4-15a, b,c.	Mutually perpendicular axes outputsfor three supply pressures	34
Figure 4-16.	Input pressure - flow characteristic	35
Figure 4-17.	Null shift vs supply pressure	36
Figure 4-18.	Null shift as a function of supply temperature	36
Figure 4-19.	FDSC noise characteristic at P_+ = 100 PSIG	37
Figure 4-20.	FDSC noise characteristic at P_+ = 200 PSIG	37

LIST OF FIGURES

		PAGE
Figure 5-1.	LARS silhouette	38
Figure 5-2.	LARS flow pattern for applied rate	38
Figure 5-3.	Laminar rate sensor output vs applied rate	39
Figure 5-4.	Power consumption as function of supply pressure	40
Figure 5-5a.	Null shift with supply pressure	41
Figure 5-5b.	Null shift with temperature	41
Figure 5-6.	HDL-LPA Model 2-2B silhouette	45
Figure 5-7.	Comparison of LARS calculated and experimental data	46
Figure 5-8.	LARS bandwidth vs supply pressure	47
Figure 5-9.	LARS gain and phase as a function of frequency	48
Figure 5-10.	Jet position under condition of maximum allowable jet deflection	49
Figure 5-11.	Cross axis sensitivities for LARS	51
Figure 6-1.	VRS output as function of applied rate	53
Figure 6-2.	Sensitivity of VRS with supply pressure	53
Figure 6-3.	VRS amplitude ratio and phase vs frequency	54
Figure 6-4.	Supply pressure-flow characteristic	55
Figure 6-5.	VRS instrument noise at P_+ = 180 PSI, ω = 0	56
Figure 6-6.	Null shift vs supply pressure	58
Figure 6-7.	Null shift vs temperature	58
Figure 6-8.	Cross-axis sensitivity	59
Figure 6-9.	Cross-axis sensitivity	59

1.0 INTRODUCTION

Since the early days of Fluidics there has been the need for angular rate sensing components.[1] [2] Through the years[3] and continuing to the present time, the need has persisted.[4] To satisfy the needs of control systems, three angular rate sensors have been prominent in their development: namely, the Fluidisc (FDSC), the Laminar Angular Rate Sensor (LARS), and the Vortex Rate Sensor (VRS). The VRS has been reported on both emperical and theoretical grounds.[5] [6] The LARS has been reported[3], but the FDSC has not yet been fully reported upon.

This report has, as its objectives, an independent assessment of the performance of all three sensors, supplementing this with detailed analyses of the FDSC and the LARS. The assessment is based on the measured characteristics of these sensors and their potential for improvement for advanced system applications. This second aspect, namely the potential for improvement, is important because the sensors which were tested are not likely to be the best of their genre, simply those available at hand.

The utility of this report is not the recorded data itself, but rather the interpretation of the data in terms which provide guidelines for future developments to enable the fluidic sensors to be competitive with other angular rate-of-turn sensors.

The organization of this report is such that the Conclusions and Recommendations are presented first, followed by supportive analyses and data.

---

[1] Design Of A Fluidic Missile Control System, Bowles Engineering Corp. Report No. R-5-20-66,1966.

[2] Mentzer, William R. "Pure Fluid Torpedo Control", Bowles Fluidics Corp. Report No. R-7-18-68.

[3] Young, R. "Feasibility Investigation Of A Laminar Angular Rate Sensor (LARS)", prepared under Contract No. N0018-72-C-0231, 1973.

[4] Neradka, V.F. "Development Of Computer Models For Fluidic Control Systems", TRITEC, INC. Report No. 7001, prepared under Contract No. DAAG39-73-C-0159, 1974.

[5] Burton, R.V. "Two Axis Vortex Rate Sensor Package", prepared by Honeywell, Inc. under Contract No. DAAG39-73-C-0159, 1974.

[6] Ostdiek, A, "Viscous Vortex Rate Sensor", HDL-TR-1555, 1971.

2.0 CONCLUSIONS AND RECOMMENDATIONS

Each of the three sensors has particular advantages and limitations as can be seen by review of the following Sections of the report. The VRS dates from the early 1960's and has had the advantage of the most developmental effort. The FDSC and the LARS were developed much later, one being an analog to the spinning mass gyro and the other being an analog to jet deflection fluidic amplifiers. The FDSC evolved because it can be used to provide high sensitivity with the ability of driving power devices of some hydraulic systems. By reducing impedance-matching fluidic elements, the FDSC appears attractive for systems wherein large temperature changes are encountered. Its chief drawback is the delicacy and expense of fabrication of the hydrostatic support bearings. The LARS came into being after the laminar fluidic amplifier. This sensor is inherently able to couple to a fluidic circuit, and offers the utmost in rate sensor cost savings.

In summary,

- With the lowest threshold and null sensitivities and intermediate output impedance, the FDSC could be the best of the three sensors if its bearings problem could be resolved. If not, this device offers little advantage over fluid supported gyros which have been used for years in control systems. The FDSC offers the possibility of directly driving power devices in some applications, and has inherent high sensitivity and low temperature sensitivity. FDSC development should focus on bearing refinement from the standpoint of ruggedness and low cost.

- The LARS sensor is the most economical sensor. In addition to low hardware cost, it has extremely low power consumption compared to the other two sensors, and it is readily coupled to fluidic circuits. Its threshold is only slightly higher than the FDSC. A problem must be overcome, however, before this sensor is truly useful. The sensor has a high null shift with temperatures and supply pressure. This can be reduced by improvement of manufacturing technology. This is

only partially satisfactory, because a truly symmetric fabrication is never possible. What is strongly recommended is the development of trim circuits to compensate for manufacturing asymmetries which give rise to pressure differentials resulting from the mix of pipe and orifice characteristic pressure drops. Such development would have a spin-off beneficial to other laminar fluidic devices as well.

- The VRS may continue to be utilized in applications where it has demonstrated system performance. The cost of the unit and the need for buffer amplification to achieve impedance-matching suggest that the VRS will not grow in useage with the advent of the FDSC and the LARS, both of which have lower threshold rates. Further development of the VRS does not appear warranted.

3.0 COMPARISON OF FDSC, LARS, AND VRS

Each of the three sensors was tested with MIL-H-5606 hydraulic fluid. The test equipment used in gathering data was an Inland Control Series 800 Rate Table, Vasco Model 913 Frequency Response Analyzer, HP 3575A Gain/Phase Meter, Model 3R Industrial Measurement and Control Flowmeter, Dores DS-350 and Cromel-Allmed Temperature Measurement System, HP 7046A Dual Channel XY Recorder and Tectronix Oscilloscope Model 5103N.

The FDSC uses deflection of a mechanical part to measure applied rate. The prime advantage of this sensor is its high sensitivity to angular rate. When powered from a flow source, the FDSC also has good supply and temperature insensitivity. The response is adequate, and the output impedance is low. There are only two detractors to the sensor. First, it has mechanical bearings which are delicate and difficult to align; and second, it is an expensive sensor when compared with the LARS. FDSC performance lies between the LARS and the VRS in output impedance, flow consumption, and cross-axis sensitivity, in spite of the fact that it has had a very short development period. If improved bearing designs can be found that are cost effective, this sensor could provide the best total performance within the limits of its moving part and cost.

The LARS is the simplest to manufacture; and significantly, it can be manufactured by those processes existing or under development for fluidics such as chemical etching or fine blanking. This breakthrough in cost is further enhanced by the low output impedance which does away with impedance-matching amplifier stages needed for the VRS. Other significant advantages include the low power consumption, size, and ease of manifolding with other fluidic components. The low sensitivity of the LARS is not a serious problem with the state-of-the-art laminar amplifiers. In order to make this statement entirely correct, however, some means must be developed to compensate for the high null shift with supply and temperature characteristics of this device.

The VRS has existed since the inception of the field of fluidics. In an approximation to the law of the conservation of angular momentum, the VRS amplifies the rate velocity component. The highly accelerating radial

flow is laminar, and the noise of the VRS is quite low. The axisymmetric flow field renders the device quite insensitive to cross-axis perturbations. The major drawback of the VRS is that in order to take advantage of the amplification due to the conservation of angular momentum, the output must be situated at a relatively small radius. The detector itself must thus be small and of high output impedance and is difficult to manufacture. Many detectors have been investigated over the years to overcome the manufacturing difficulties, and none have met with success. The output impedance has merely been accepted, and applications with the VRS invariably require impedance-matching amplifiers.

The remainder of Section 3 compares the performance of each of the sensors in areas of concern to the system designer. Sections 4, 5, and 6 include a development of the analysis of the individual sensors.

3.1 Sensitivity

The greatest sensitivity is obtained with the FDSC as can be seen from Figure 3-1. This contributes to the lesser null shift with pressure of the FDSC as shown in Figure 3-2. The LARS has far less sensitivity than either of the other two sensors. Consistent with Reference 3, the LARS also has high null shift with supply pressure. One of the features which makes the LARS attractive despite its low sensitivity and high null shift is its low power consumption, as can be seen from Figure 3-3.

3.2 Bandwidth

The bandwidth of the three sensors varies considerably between units. The measured bandwidths are shown in Table 3-1.

TABLE I. SUMMARY OF SENSOR BANDWIDTHS

SENSOR	BANDWIDTH (MEASURED)	BANDWIDTH (CALCULATED)
FDSC	3 Hz	82 Hz
LARS	10 Hz	19 Hz
VRS	10 Hz	15 Hz

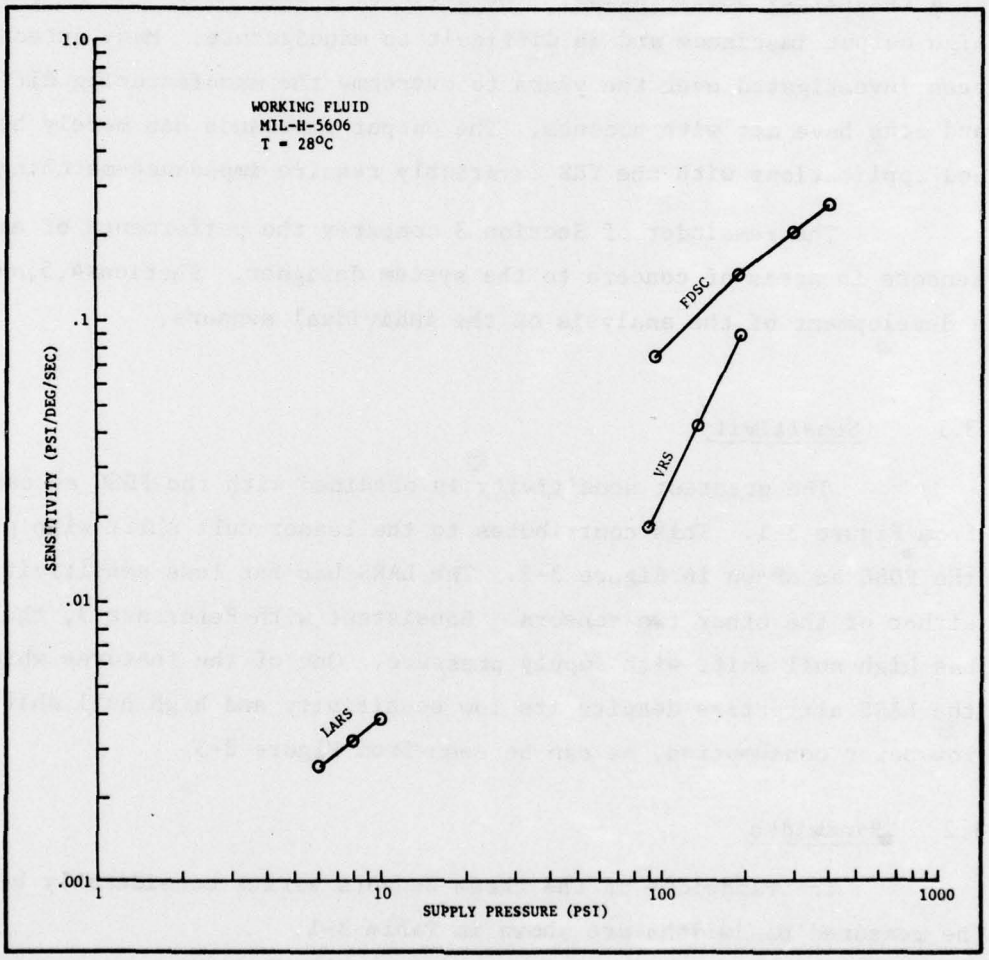

Figure 3-1. Sensitivity vs supply pressure

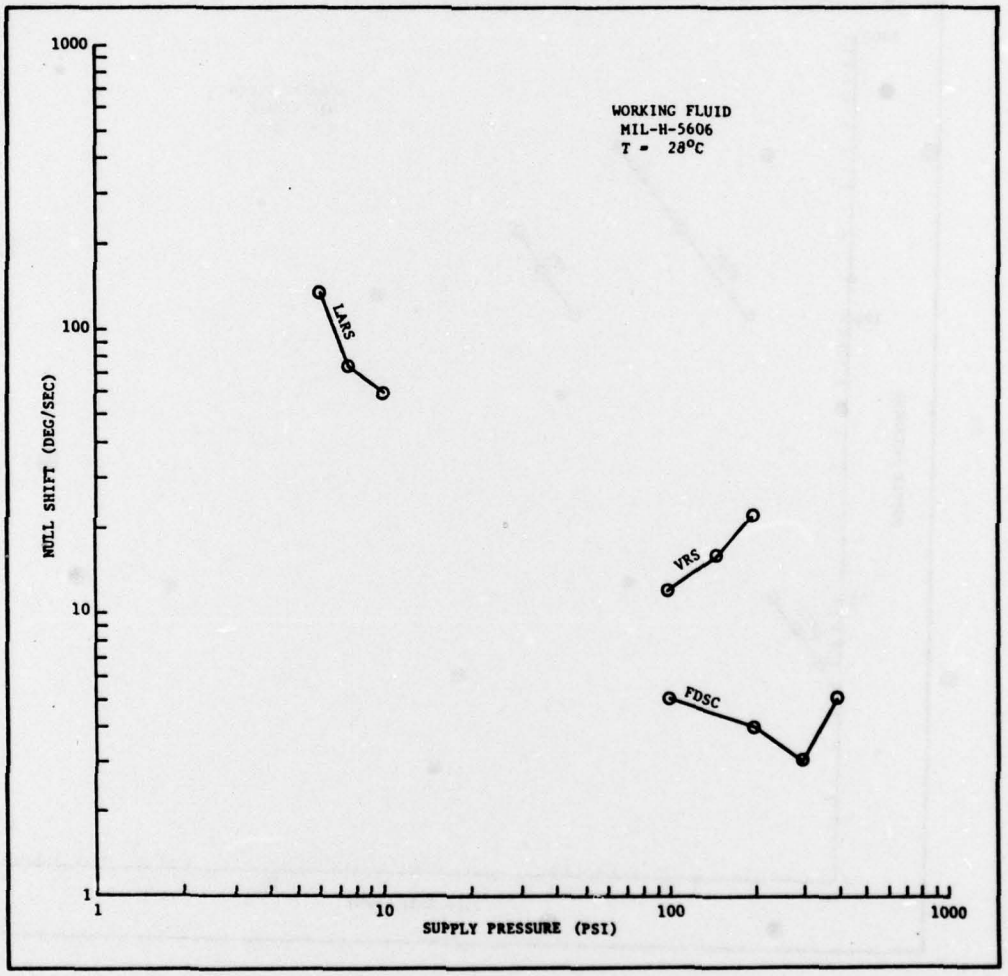

Figure 3-2. Null shift vs supply pressure

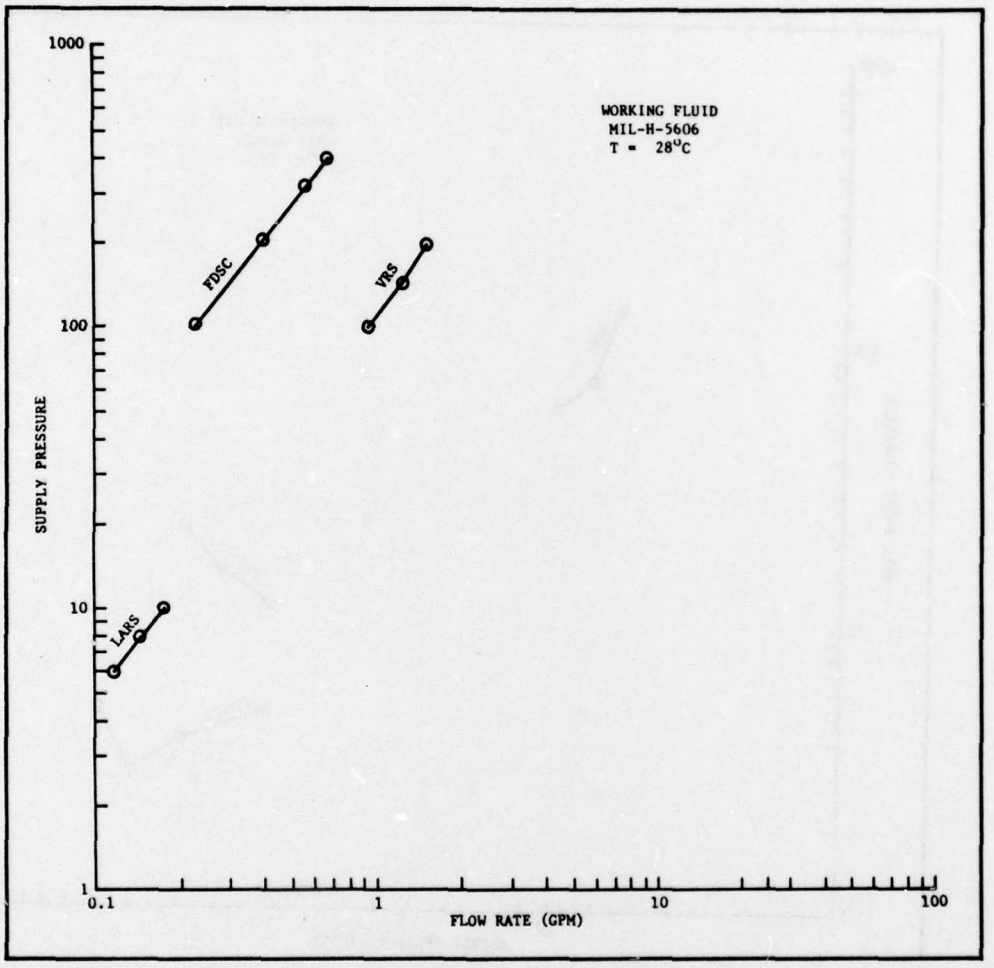

Figure 3-3. Supply pressure vs flow rate

The agreement between theory and experiment is poor. For the FDSC it appears that the discrepancy is one of experimental arrangement and damaged rotor bearings. This bearing problem points to a disadvantage of a moving part sensor such as the FDSC as compared to the two other sensors. The factor of two disparity between LARS calcuated and measured is attributed to the simplicity of the mathematical model.

3.3 Null Shift

The null shift arising from supply pressure was shown in Figure 3-2. Figure 3-4 shows null shift as a function of temperature. Once again, the FDSC has the least and the LARS the most null shift. The maximum rate that can be sensed with the LARS, however, suggests that it may be most applicable to those systems of high rotational speed.

3.4 Cross-Axis Sensitivity

Figure 3-5a,b, shows the cross-axis sensitivity of each of the three sensors. About the Y axis, (See Figure 3-6), the FDSC and the LARS are comparable in terms of percent of the sensitive axis signal. The cross-axis VRS sensitivity is noticeably less. About the Z axis, the FDSC is less sensitive to this off-axis rotation than the LARS, and the VRS has immeasurably small sensitivity to an off-axis input.

3.5 Output Impedance

The output impedance ranges of each of the three sensors are:

Z_o (FDSC) = 100 psi/cis
Z_o (LARS) = 20-30 psi/cis
Z_o (VRS) = 400-800 psi/cis

The extremely high value of the VRS causes difficulty in matching with other system components, whereas the problem does not exist with the FDSC and LARS.

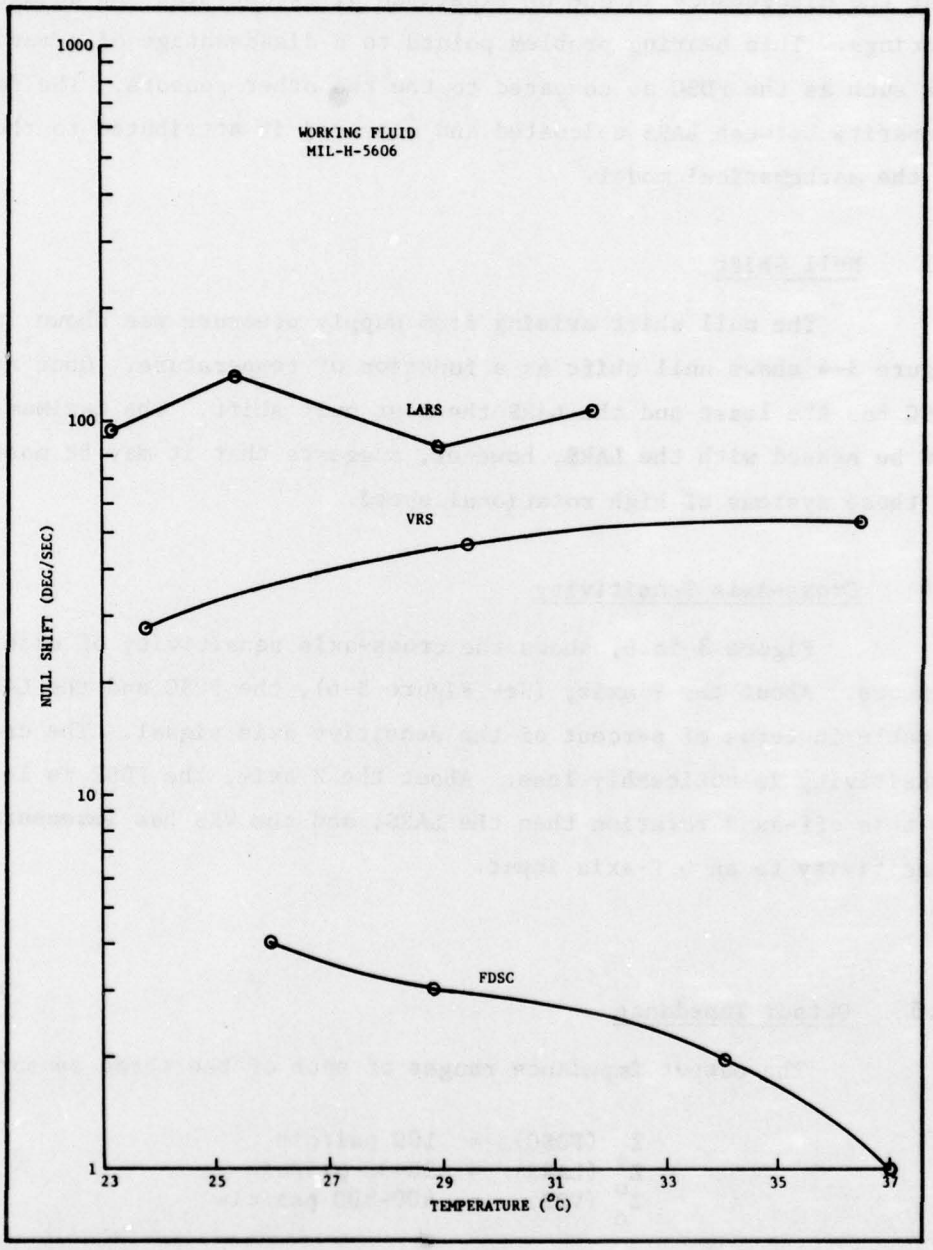

Figure 3-4. Null shift vs temperature

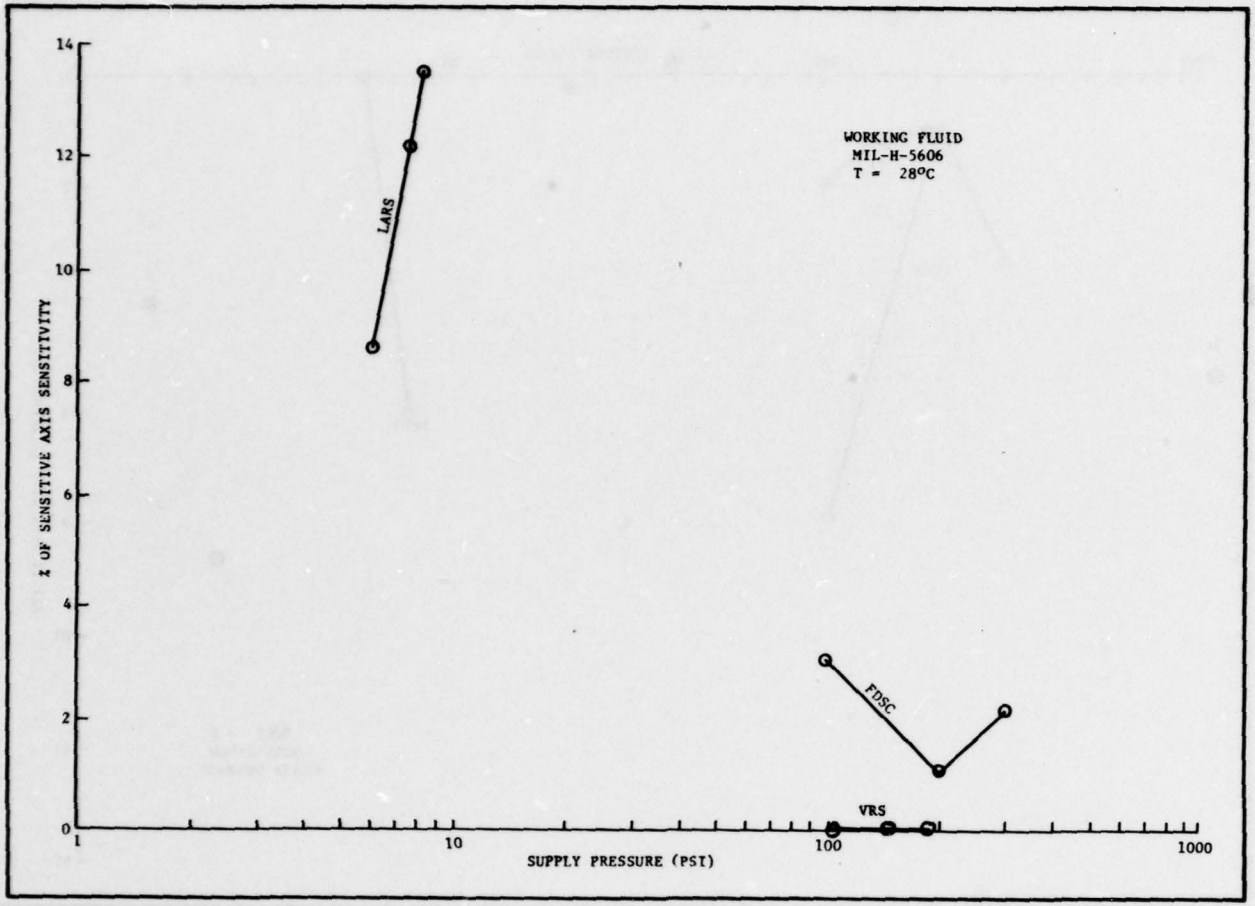

Figure 3-5a. Cross-axis sensitivity (Z axis)

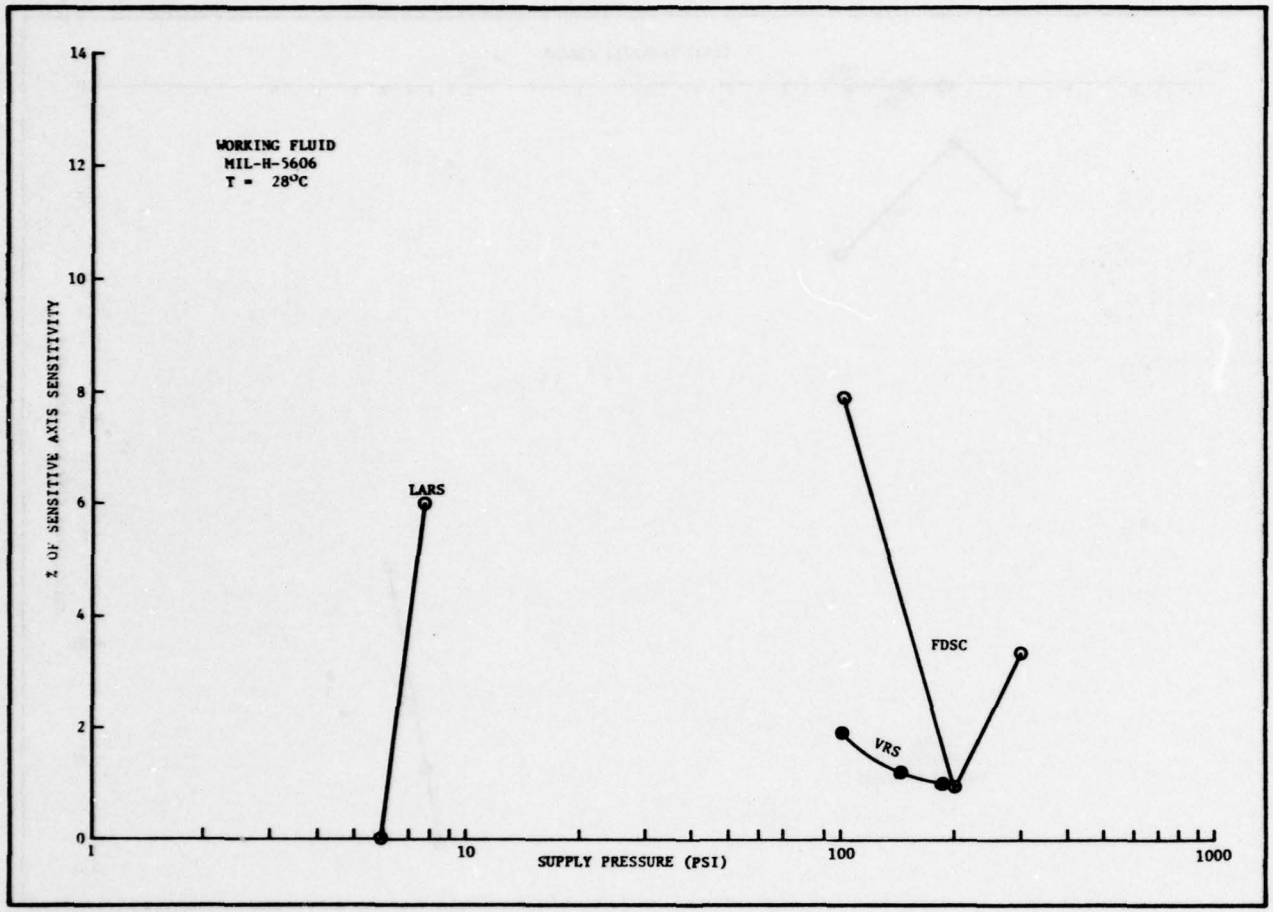

Figure 3-5b. Cross-axis sensitivity (Y axis)

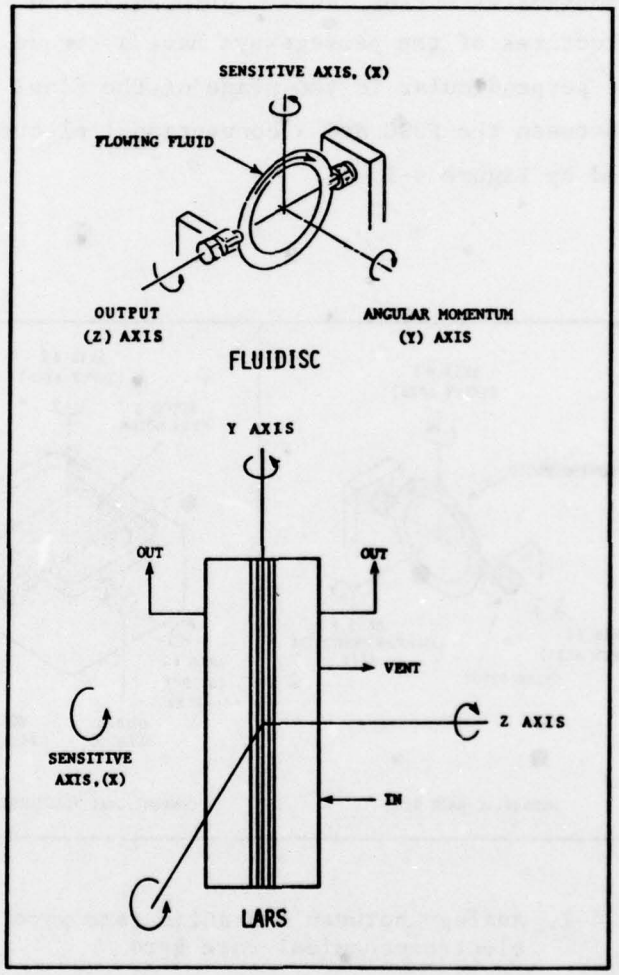

Figure 3-6. Cross-axes of LARS and FDSC

4.0 FLUIDISC RATE GYRO ANALYSIS

The FDSC has as its operating principle the gyroscopic action of a spiral passageway of moving fluid. When subjected to an applied rate of turn, the structures of the passageways have a torque impressed upon them about an axis perpendicular to the plane of the flow. The direct analogy that exists between the FDSC and a conventional electromechanical rate gyro is illustrated by Figure 4-1.

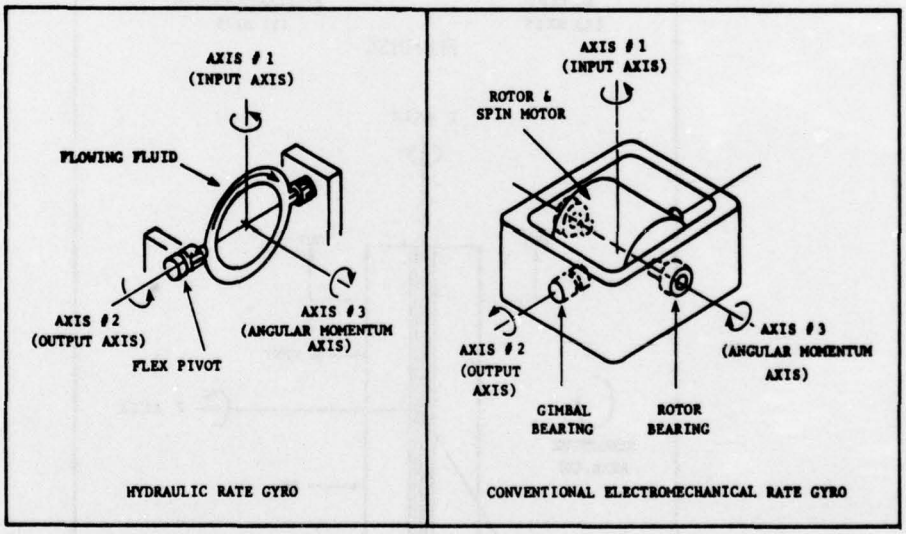

Figure 4-1. Analogy between hydraulic rate gyro and conventional electromechanical rate gyro

The sensor output is derived from the pressure differential required to counterbalance the torque applied to the passageway structure as a result of an applied rate. This ΔP is sensed through a flapper nozzle arrangement as shown in Figure 4-2.

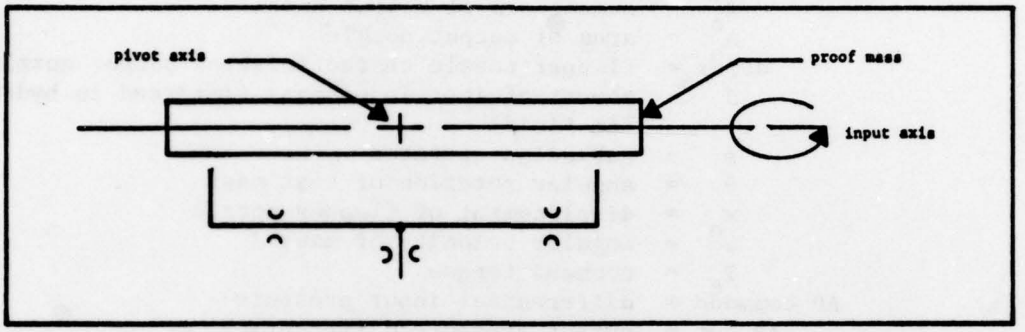

Figure 4-2. Flapper nozzle general arrangement

In the actual hardware, two sets of nozzles act on the proof mass. One provides feedback restoring torque to null out the inertial acceleration of the mass, and to provide the ΔP output signal proportional to the displacement of the mass in equilibrium with the torquing nozzles. The second provides the capability of applying command torque input from a differential pressure signal. Both sets of nozzles are a flapper nozzle pair.

Summing torques about the pivot axis, the block diagram of the system is shown to be

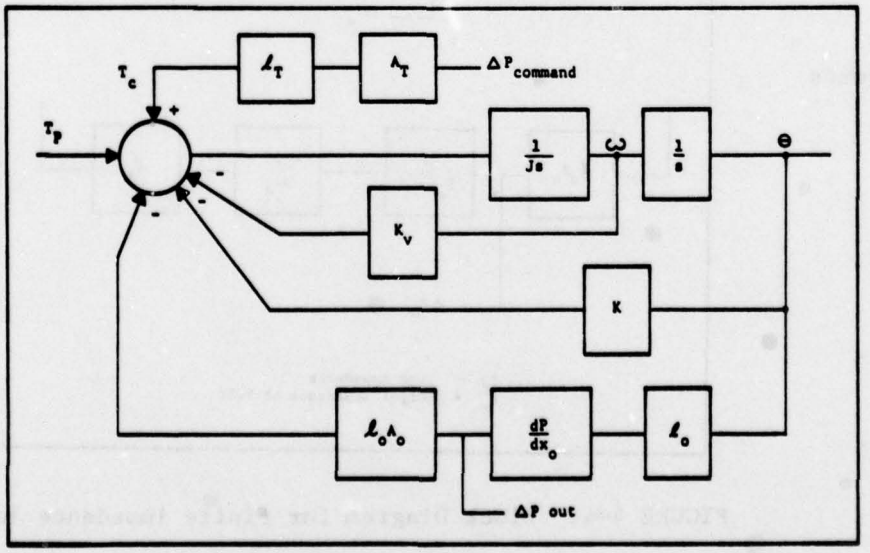

Figure 4-3. Block diagram of FDSC

where T_p = torque applied about pivot axis
K^v = viscous damping
K^v = spring rate of bearing support
ℓ_T = moment arm of torquing nozzle
A_T = area of torquing nozzle
ℓ_o = moment arm of output nozzle
A_o = area of output nozzle
dP/dx_o = flapper nozzle characteristics output nozzle
J = moment of inertia of mass (immersed in hydraulic fluid)
s = LaPlacian operator
θ = angular rotation of test mass
x_o = displacement of flapper nozzle
ω_o = angular velocity of mass J
T_c = command torque
ΔP command = differential input pressure
ΔP out = output pressure differential

For dead-headed load, (the condition of the tests) the preceding block diagram is valid. Under the condition of driving a finite impedance, two modifications must be made to the system representation. The portion of the circuit represented by

becomes

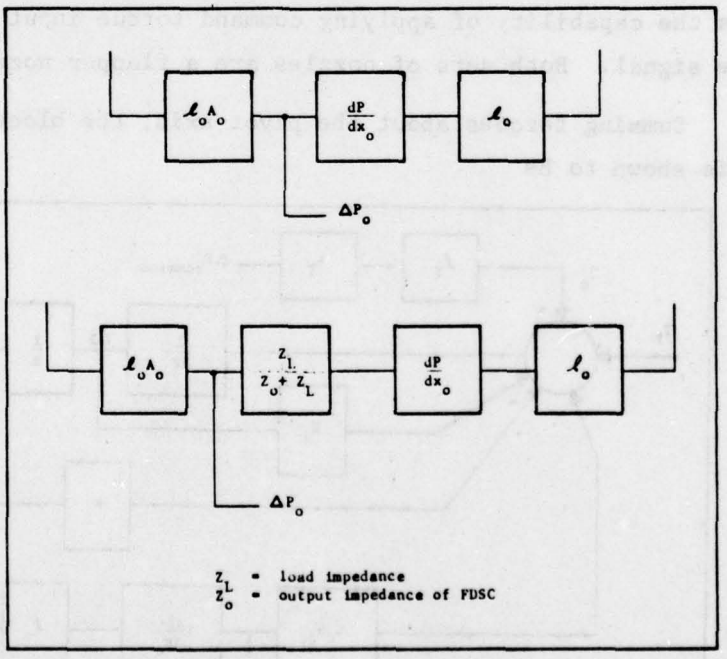

FIGURE 4-4. Block Diagram for finite impedance load

The test was performed for $Z_L = \infty$, and hence each of the impedance blocks become unity. Reducing the block diagram for blocked load yields

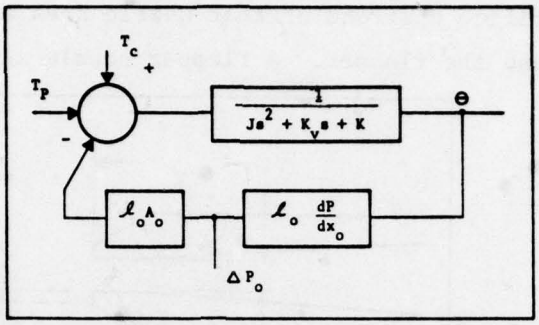

Figure 4-5. FDSC block diagram reduction

Further reduction of the block diagram shows that for $T_c = 0$

$$\frac{\Delta P_o}{T_P} = \frac{\ell_o \frac{dP}{dx_o}}{Js^2 + K_v s + K + \ell_o^2 A_o \frac{dP}{dx_o}} \qquad (1)$$

The torque about the pivot axis is related to the angular rate applied about the input axis by

$$T_P = H\,\Omega = \frac{2\pi r^2 N w \Omega}{g} \qquad (2)$$

where
- Ω = applied input rate
- H = angular momentum of fluid through the spirals
- r = effective radius of flow passageways
- w = flow rate
- N = number of spirals comprising flow passageay
- g = acceleration of gravity

Introducing this into the transfer function gives the complete linear representation of the FDSC rate gyro

$$\frac{\Delta P_o}{\Omega} = \frac{\frac{2\pi}{g} \ell_o \frac{dP}{dx_o} r^2 N w}{Js^2 + K_v s + (K + \ell_o^2 A_o \frac{dP}{dx_o})} \qquad (3)$$

which can be redefined as

$$\frac{\Delta P_o}{\Omega} = \frac{C_1}{Js^2 + K_v s + C_2} \qquad (4)$$

4.1 Flapper Nozzle Considerations

The flapper characteristic dP/dx_o depends not only on A_o but also on a fixed orifice upstream of that nozzle area and the gap between the exit plane of A_o and the flapper. A flapper nozzle is shown below

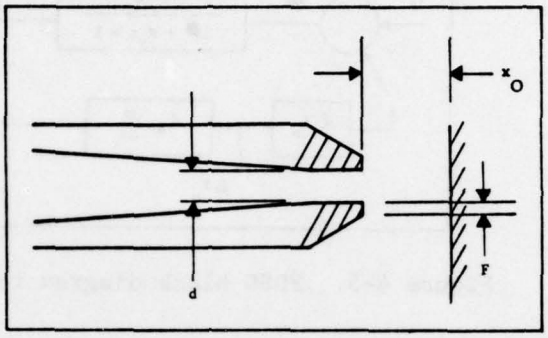

Figure 4-6. Flapper nozzle

The flapper will function as a pure orifice as long as $x_o < d/5$. Ideally, $F < x_o$ min. Since F = 0.010 in., x_o must be greater than 0.010 in. It is improbable that the torquing nozzles can be made sharp enough to eliminate all non-linearities in the system. At small x_o the nozzle behaves as a flat-faced nozzle as shown below

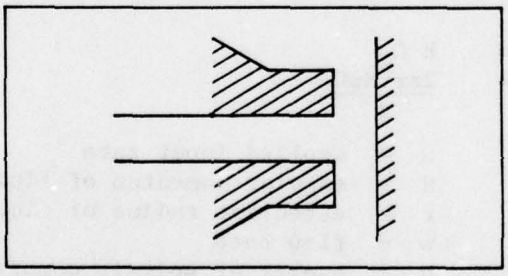

Figure 4-7. Flat-faced flapper nozzle

As soon as the resistance to the flow of the radial sheet of fluid between the flapper and the nozzle end becomes appreciable compared to that the nozzle orifice and the flow characteristic departs from the true orifice law and begins to approach the linear, laminar flow law. Once the laminar portion of the

resistance is the controlling factor, the flow varies as x_o^3 rather than x_o. Flow also becomes inversely proportional to the viscosity of the fluid. Because the nozzle as fabricated is quite flat-faced, the nozzles can be expected to contribute to temperature and pressure sensitivities.

For the purpose of analysis, it will be assumed that the flapper nozzle behaves like an orifice. Its characteristic is therefore given by

$$\frac{P_1 - P_2}{P_o - P_2} = \frac{1}{\left(\frac{A_2}{A_1}\right)^2 + 1} \tag{5}$$

where P_o = upstream pressure (supply)
P_1 = intermediate pressure (signal)
P_2 = downstream pressure (ambient)
A_1 = upstream orifice effective area
A_2 = downstream orifice effective area

In the linear range of this function, the following simplification is possible (See Figure A-8 in Appendix A)

$$\frac{P_1 - P_2}{P_o - P_2} = -0.6\,\frac{A_2}{A_1} + 1.1 \tag{6}$$

$A_2 = \pi d x_o = \pi(0.043)x_o \approx 0.135 x_o$ in.^{2}, x_o being the nominal gap between the nozzle and flapper. Then

$$\frac{P_1 - P_2}{P_o - P_2} = \frac{-0.6\,(0.135)x_o}{A_1} + 1.1 \tag{7}$$

P_2 is taken as a reference, and $A_1 = 1.327 \times 10^{-4}$ in.^{2} from direct measurement of the hardware. The slope of the curve in the linear portion of the curve is

$$\frac{dP_1}{dx_o} = 610\,P_o \tag{8}$$

4.2 Sensitivity

The flapper nozzle data, the physical parameters, and flow rate enable a determination of the steady state gain. Measurement of the hardware

shows ℓ_o = 1.4 in., r = 1.25 in., and therefore, $A_o = 0.043\ x_o$. Substituting the values obtained thus far into the transfer function, equation 4

$$C_1 = \frac{2\pi \ell_o}{g} \frac{dP}{dx_o} r^2 N w = 91 P_o w \tag{9}$$

$$C_2 = \ell_o^2 A_o \frac{dP}{dx_o} = 161 P_o X_o \tag{10}$$

The steady state gain, C_1/C_2 is independent of P_o but varies with flow through the spiral and flapper nozzle gap x_o

$$\frac{C_1}{C_2} = 0.56\ w/x_o \tag{11}$$

For a flow rate of w = 0.099 lb/sec which was measured at 200 psi in the tests, $C_1/C_2 = 2.74 \times 10^{-2}/x_o$. The precise value of x_o is not known. GE reports that x_o = 0.0050 in. and x_o = 0.0035 in. These values of x_o put the range of C_1/C_2 as $5.5 < C_1/C_2 < 7.85$. This can be verified as can the linearity of the response from the data of Figure 4-8 which is the FDSC output as a function of applied rate.

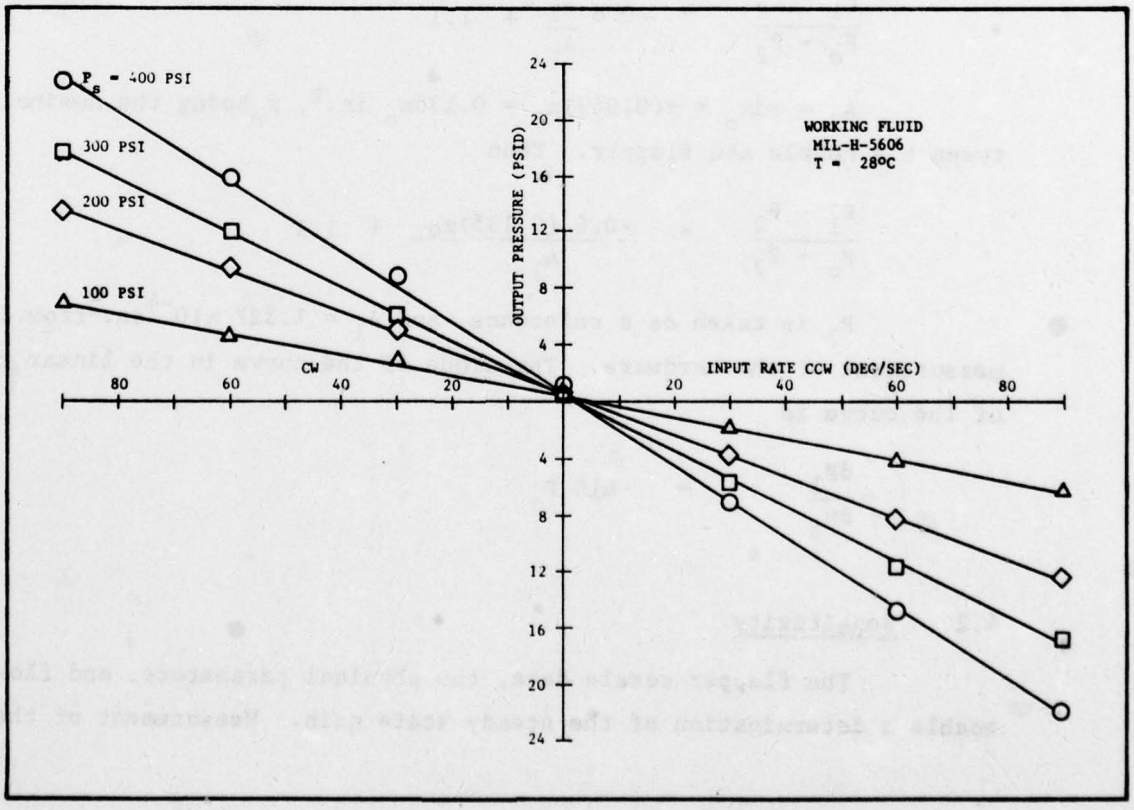

Figure 4-8. FDSC output vs applied rate

Plotting the slopes of the curves of Figure 4-8 , as shown in Figure 4-9 gives the steady state gain, or sensitivity as a function of supply pressure. At 200 psi, the measured value is 0.15 psi/deg/sec.

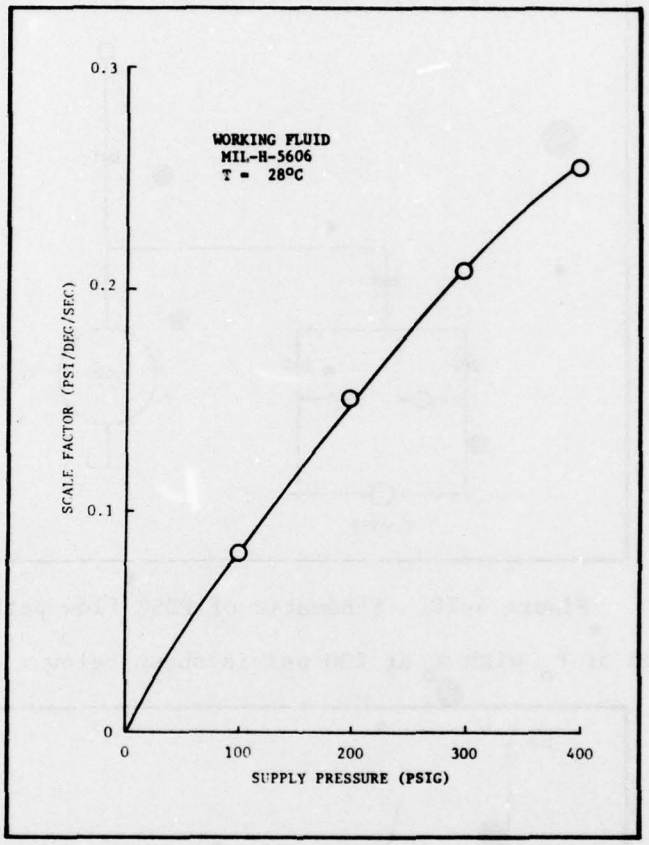

Figure 4-9. FDSC scale factor vs supply pressure

If one can conclude that x_o = 0.0035 in. is correct, the correlation between theory and experimental verification is within 10%.

4.3 Bandwidth

From an analysis of the resistance network of the FDSC, shown schematically as:

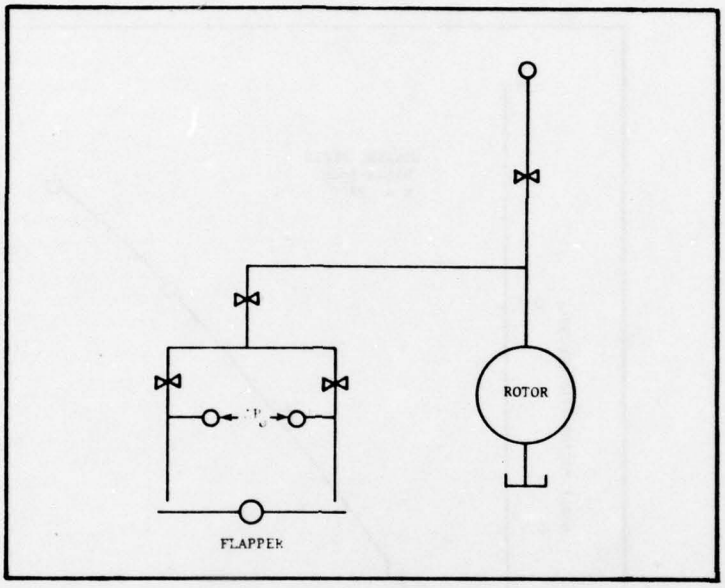

Figure 4-10. Schematic of FDSC flow path

The variation of P_o with x_o at 200 psi is shown below

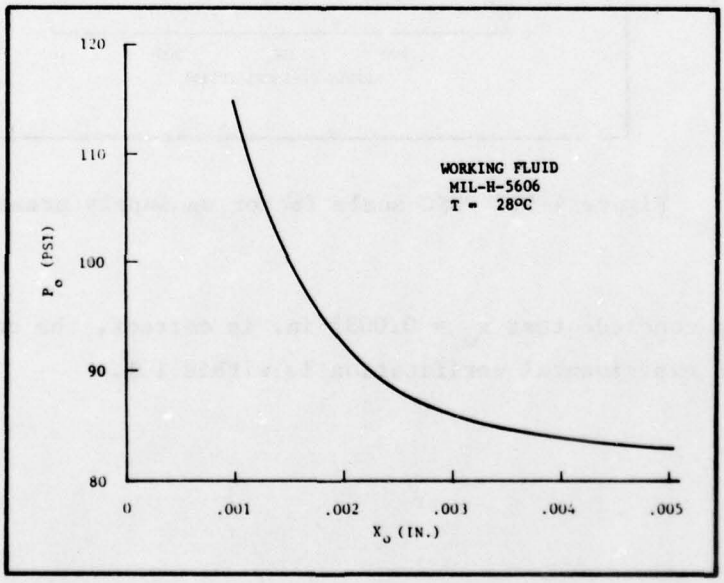

Figure 4-11. Variation of flapper output pressure with gap

For the value of x_o = 0.0035 in., P_o = 85 psi. Therefore, C_2 = 47.9. The value of J is estimated to be that resulting from four aluminum spirals plus two aluminum cover plates. The spirals are

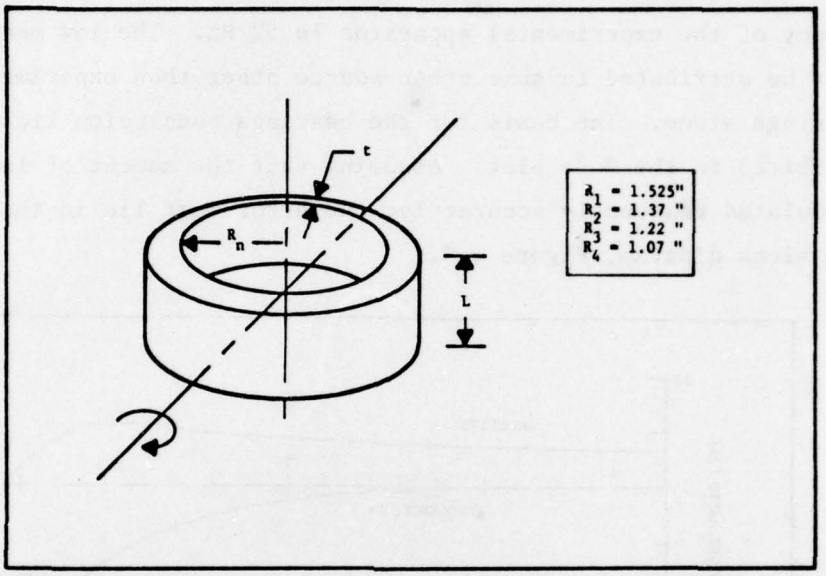

Figure 4-12. Dimensions of the aluminum boundaries to the spiral flow passageways

From this mass, the moment of inertia about the axis of rotation is given by

$$J = 2\pi\rho L R_n t \left(\frac{L^2}{12} + \frac{R^2}{2} \right) \tag{12}$$

The density is that of aluminum immersed in the hydraulic fluid, or ρ = (5.3 - 1.45) slug/ft.^{3}

$$J = J_1 + \ldots J_4 = 1.8\text{x}10^{-4} \text{ lb in.sec}^2 \tag{13}$$

The natural frequency is therefore

$$\omega_n = \sqrt{\frac{C_2}{J}} = 515.8 \text{ rad/sec} = 82 \text{ Hz} \tag{14}$$

This value of ω_n far exceeds the measured value (Figure 4-3) of 3 Hz. Only a portion of this discrepancy in natural frequency can be attributed to experimental shortcomings of the pressure transducer. The combined capacitance of the volume of the transducer and the compliance of the transducer volume is

$$C = \frac{V\gamma}{\beta} + 3\text{x}10^{-5} \text{cis/psi}^* \tag{15}$$

* $C = 3\text{x}10^{-5}$ cis/psi is the capacitance quoted by Pace for 10 psi range plate.

In hydraulic systems, $\beta \simeq 50 \times 10^{3}$ psi to account for dissolved air in the oil. Assuming a total volume of hydraulic fluid from the sensor into the transducer of 1 $in.^{3}$, C = 3.06×10^{-5} cis/psi. The FDSC output impedance is in the order of Z_o = 100 psi/cis, and therefore, RC = 3.05×10^{-3} sec, from which the break frequency of the experimental apparatus is 52 Hz. The low measured break frequency must be attributed to some other source other than experimental error and bad bearings alone. The basis for the bearings conclusion lies in the overshoot exhibited in the Bode plot. Assuming that the moment of inertia has been calculated reasonably accurately, the error must lie in the spring rate term of the block diagram, Figure 4-3.

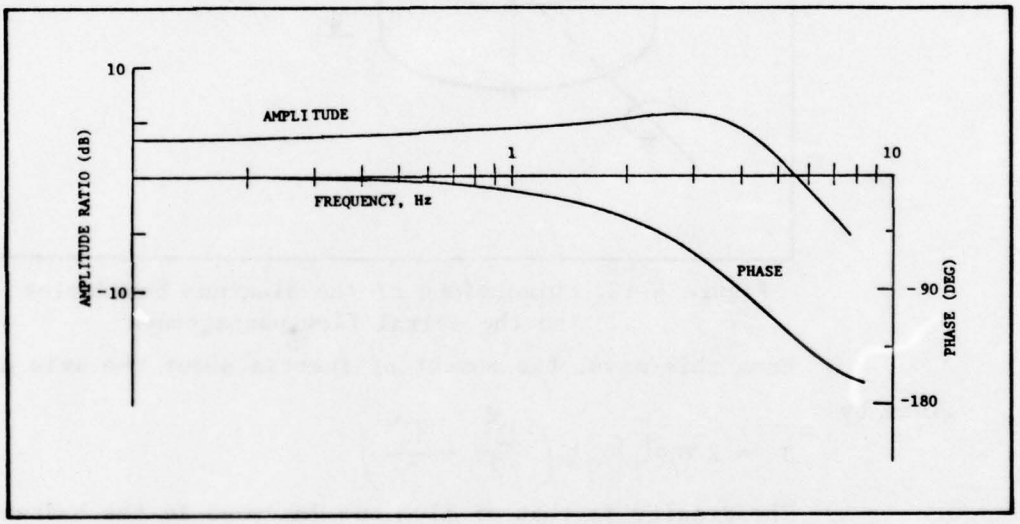

Figure 4-13. FDSC frequency response plot

At the beginning of this section it was stated that there were two flapper nozzles acting on the rotating mass. One set is the sensing nozzles and the second set is the command torquing nozzles. During the tests, it was assumed that the command torquing nozzles were to accept a command such as from a pilot input device or hand control, and be zero when such an external input was absent. If however, these torque nozzles are

supplied with a DC flow at these times, a second spring rate exists in the system, as can be seen from the block diagram below

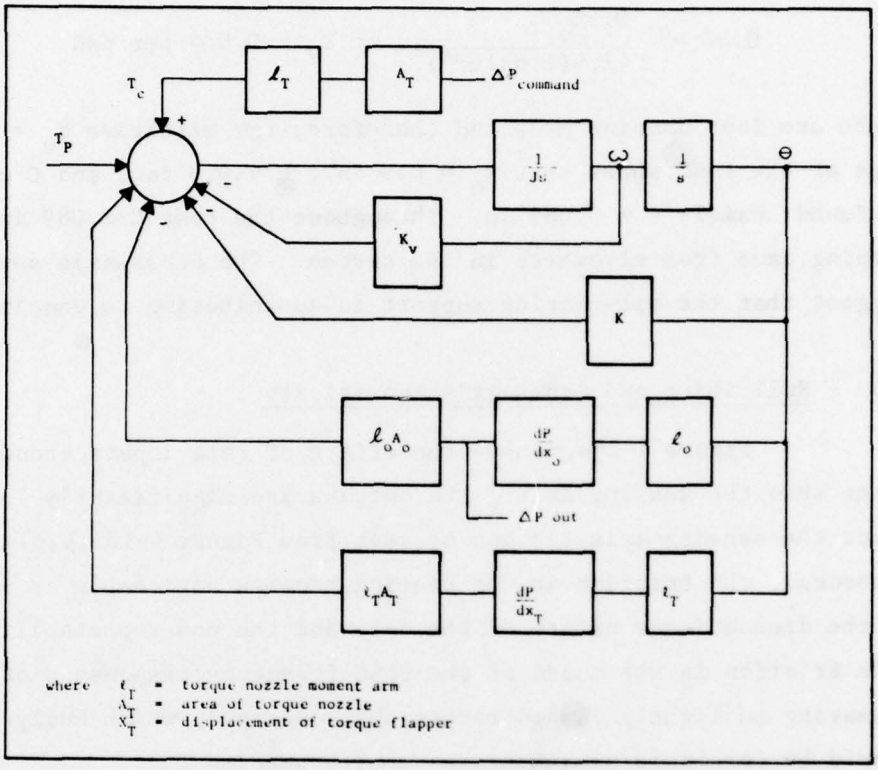

Figure 4-14. FDSC block diagram with torquing nozzles

Reducing this block diagram gives a new spring rate which will bring the experimental data into better agreement with the mathematical prediction.

The damping coefficient of a squash-plate damper such as incorporated in the FDSC is given by:

$$K_v = \frac{4.5 \mu R_o^4 L^2}{\pi^3 C^3} \qquad (16)$$

where μ = viscosity of fluid, lb/sec/in.^{2}
R_o = radius of damping disc, in.
C^o = spacing between rotor and damping disc, in.
L = moment arm of damper, in.

From the percent overshoot experimentally recorded in Figure 2-5, $\zeta \simeq 0.4$. From previous results $C_2 = 47.9$, and J has been been estimated at 1.8×10^{-4} lb in.sec. Therefore, the damping can be found from

$$0.4 = \frac{0.5K_v}{47.9(1.8 \times 10^{-4})}, \text{ or } K_v = 0.074 \text{ per pad} \qquad (17)$$

There are four damping pads and therefore, the effective $K_v = 0.296$. Drawings of the FDSC shows that $R_o = 0.5$ in., L = 0.9 in., and C can therefore be found; namely C = 0.089 in. Throughout the test C<0.089 in., which means damping came from elsewhere in the system. The cross-axis sensitivity tests suggest that the oil-bearing support is contributing to damping.

4.4 Null Shift and Cross-Axis Sensitivity

Figure 4-14a,b shows the effect of rate inputs around the two axes other than the sensing axis. The outputs are significantly lower than that about the sensing axis (as can be seen from Figure 4-15a,b,c). With these lower pressures, the friction in the bearing becomes noticeable as static friction by the discontinous nature of the data and the non-repeatability of Figure 4-14b. This friction is the cause of the FDSC frequency response plot (Figure 4-12) appearing as lightly damped rather than undamped, which analysis predicts it should be for large squash plate damping spacing C.

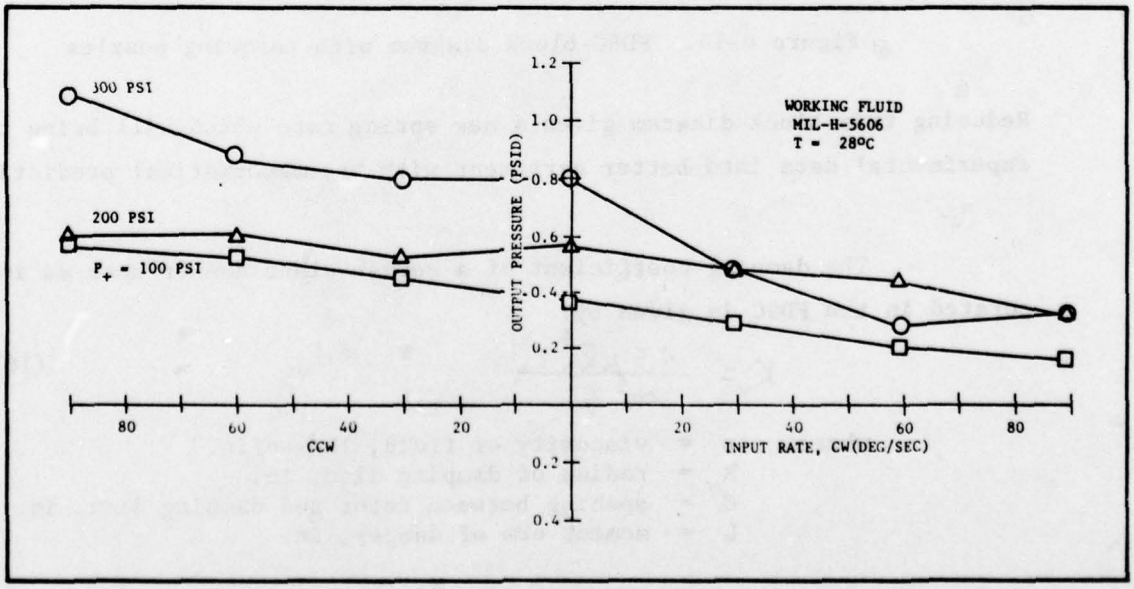

Figure 4-14a. "Output axis" cross-axis sensitivity

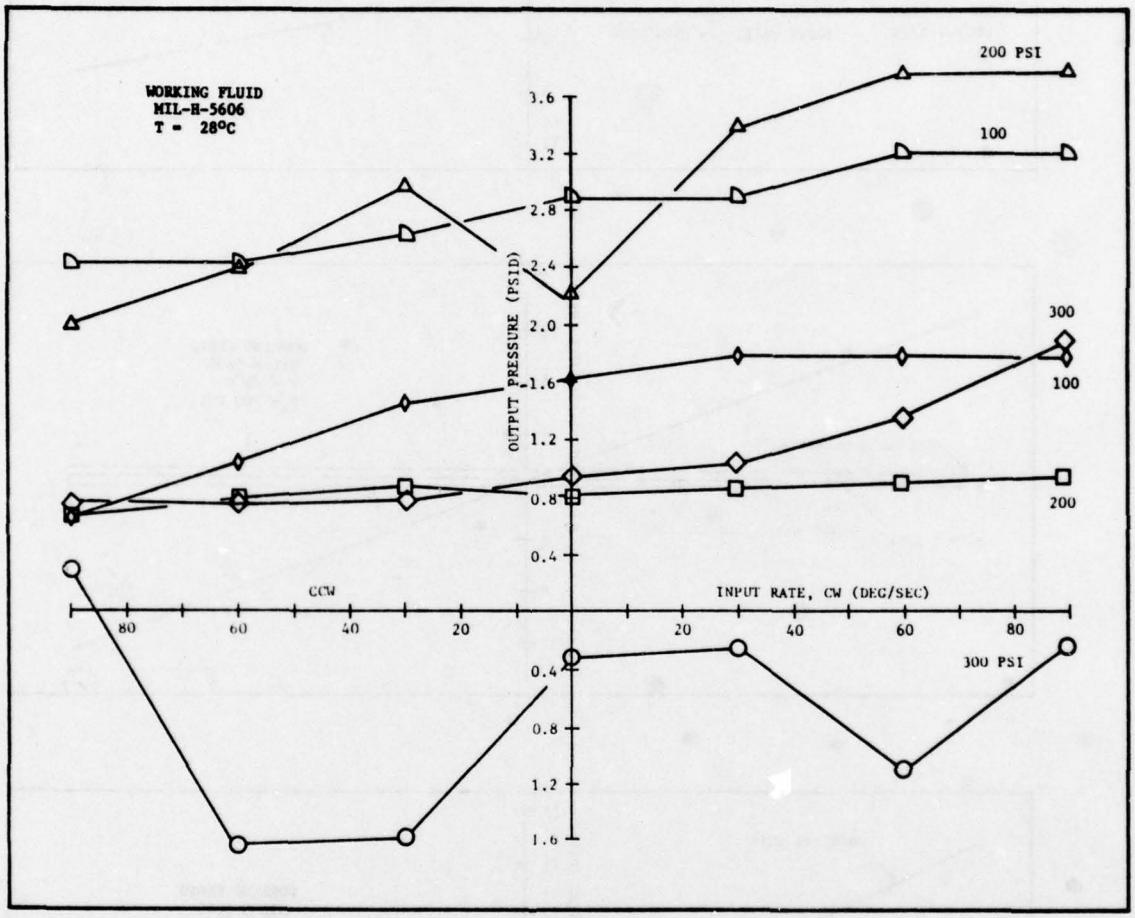

Figure 4-14b. "Angular momentum" cross-axis sensitivity for two test runs

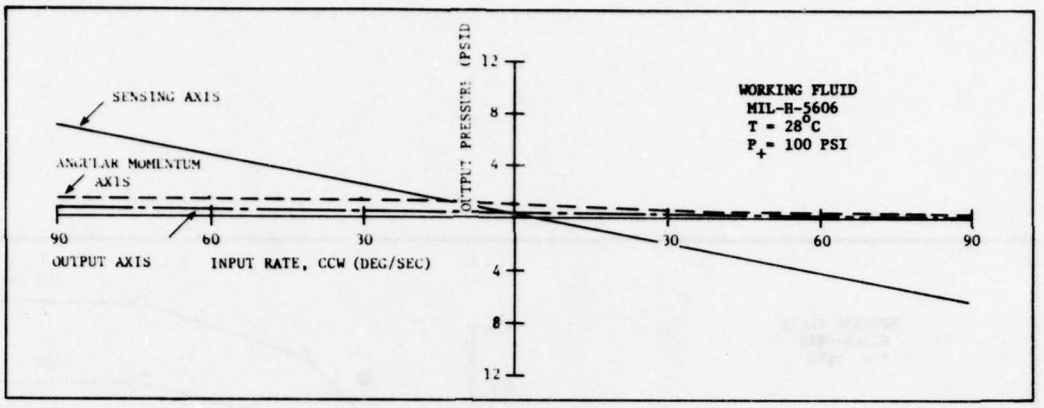

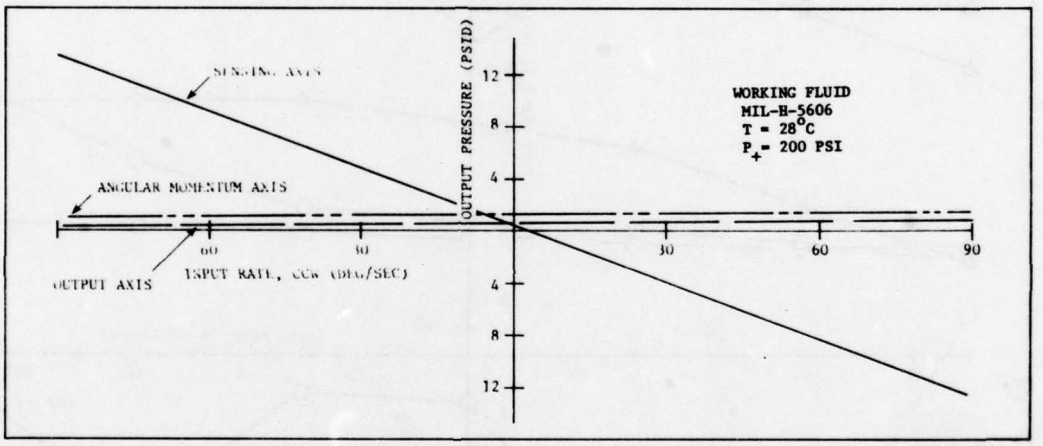

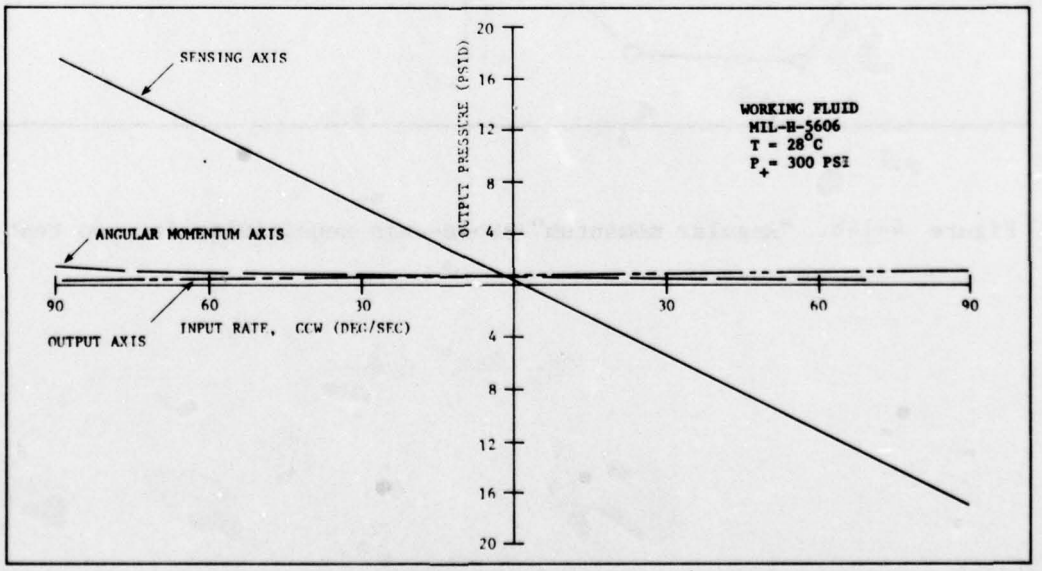

Figure 4-15 a,b,c. Mutually perpendicular axes outputs for three supply pressures

4.5 Supply Pressure and Flow Characteristics

The pressure flow characteristics for the FDSC unit which was tested is shown in Figure 4-16.

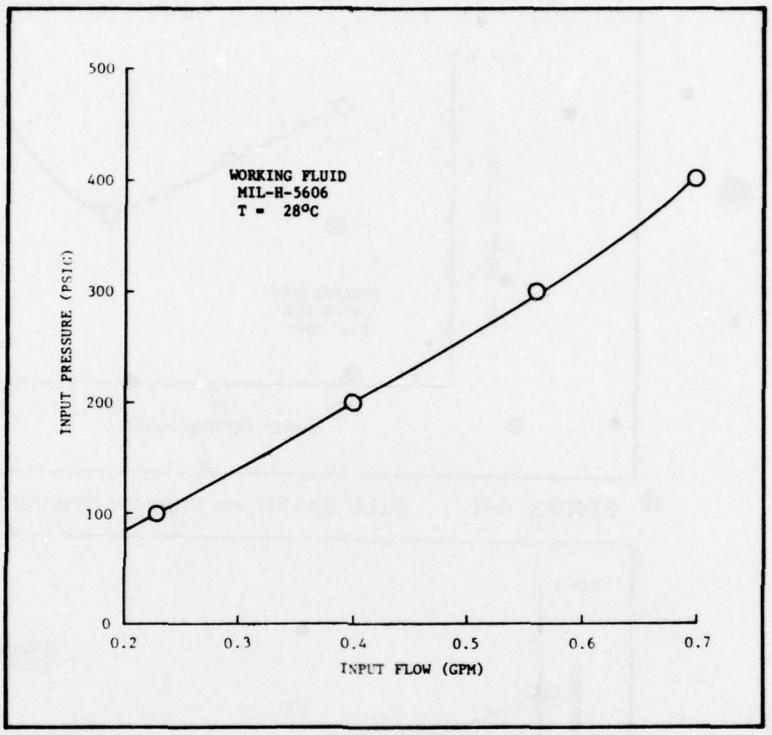

Figure 4-16. Input pressure-flow characteristic

The characteristic of Figure 4-16 for $P_+ \leq 300$ psi illustrates that of a laminar flow pressure drop up to approximately 300 psi. The laminar flow has a thicker boundary layer than would a turbulent boundary layer in the spiral. This, for an average flow rate, reduces the accuracy of the expression $T_P = H\Omega$, equation 2.

The null shift versus supply pressure shown in Figure 4-17 suggests that operation is least sensitive to supply pressure variation around 300 psi. This type of behavior is characteristic of flow related phenomena, and although never eliminated, can be reduced by proper geometry of flow passages in the vicinity of the torquing nozzles and bearing supports. During assembly of the unit prior to testing it was observed that there was considerable play in the bearing support block of the rotor and this can contribute to mechanical

asymmetry. Figure 4-18 shows the null shift as a function of supply temperature variation. Unlike the null shift variation with supply pressure, the null shift with temperature is monotonic.

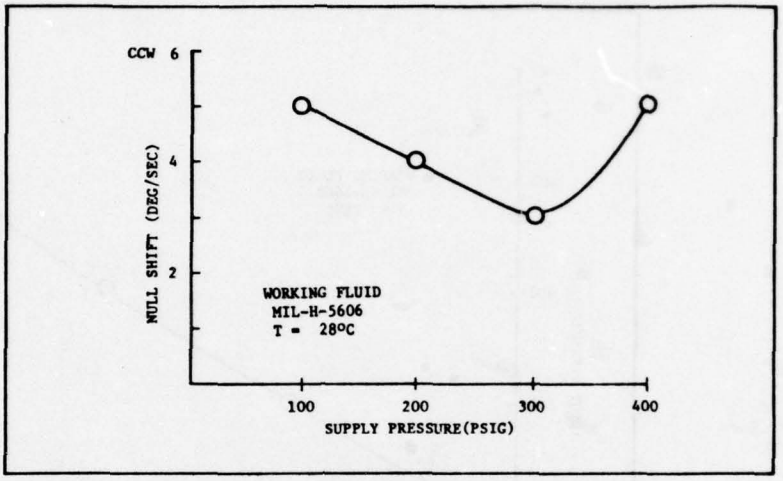

FIGURE 4-17. Null Shift vs supply pressure

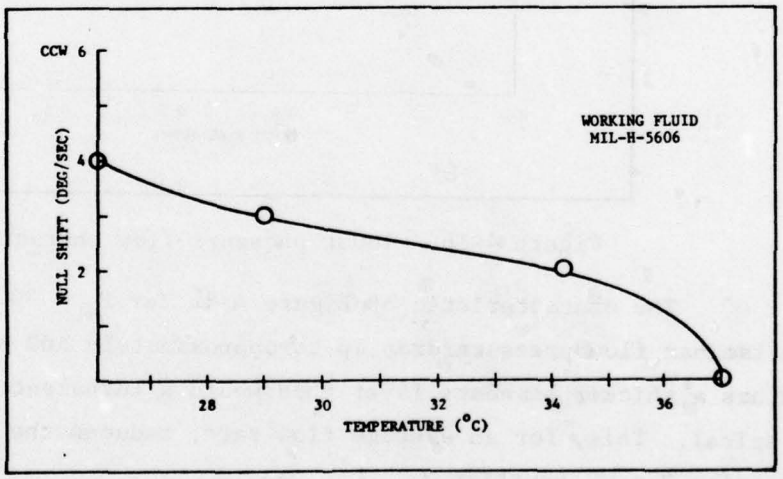

FIGURE 4-18. Null shift as a function of supply temperature

4.6 Threshold

Oscilloscope traces of the FDSC output pressure fluctuation (i.e. noise) were recorded at supply pressures of 100 and 200 psi and rates of turn at 30, 60, and 90 degrees per second. The oscilloscope traces are reproduced in Figure 4-19 and 4-20 respectively. Their effect on performance is minimal as can be seen by comparison of the signal levels of Figure 4-8 with the noise peak to peak fluctuations. The threshold, defined as the rate of turn at which the output signal equals the noise, is 0.12 deg/sec for 100 psi supply.

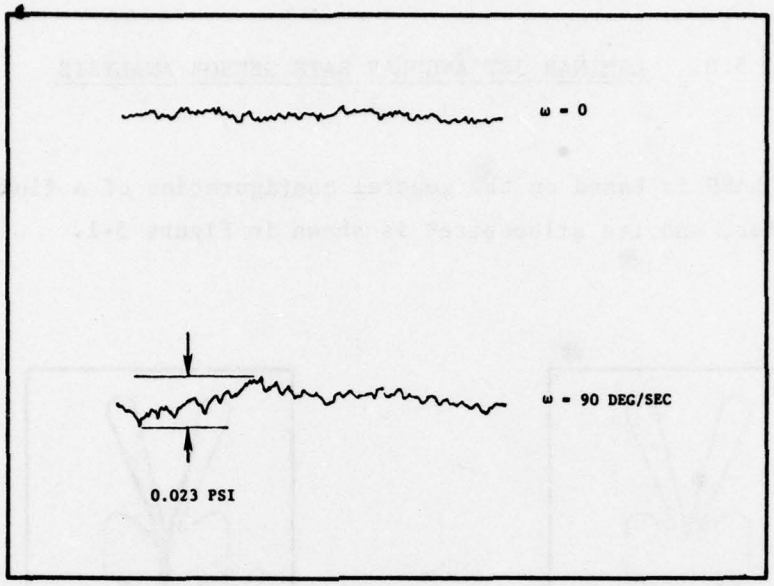

Figure 4-19. FDSC noise characteristic at P_+ = 100 PSIG

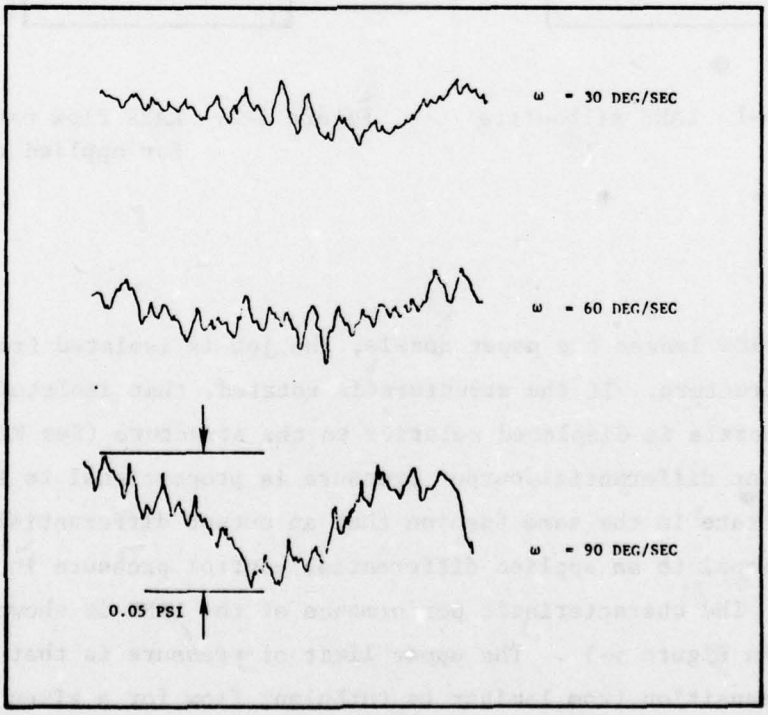

Figure 4-20. FDSC noise characteristic at P_+ = 200 PSIG

5.0 LAMINAR JET ANGULAR RATE SENSOR ANALYSIS

LARS is based on the general configuration of a fluidic laminar amplifier, and its silhouette* is shown in Figure 5-1.

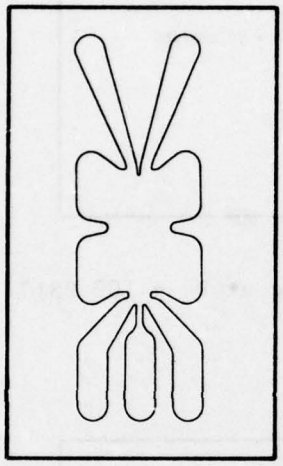

Figure 5-1. LARS silhouette

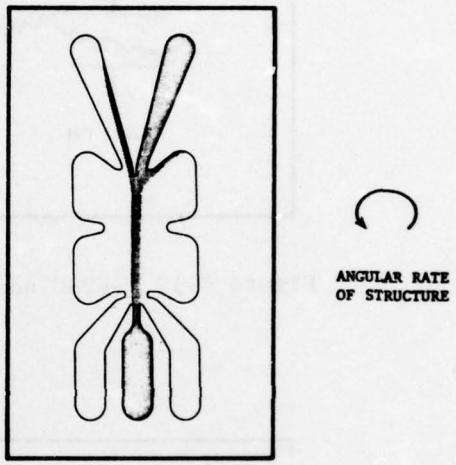

Figure 5-2. LARS flow pattern for applied rate

After the flow leaves the power nozzle, the jet is isolated from the surrounding structure. If the structure is rotated, that isolated flow from the power nozzle is displaced relative to the structure (See Figure 5-2). The resultant differential output pressure is proportional to the applied rotational rate in the same fashion that an output differential pressure is proportional to an applied differential control pressure in a fluidic amplifier. The characteristic performance of the LARS is shown for several pressures in Figure 5-3 . The upper limit of pressure is that which results in transition from laminar to turbulent flow for a given nozzle size.

---

* HDL Model No. I.R.I.004-20b_s

This pressure is related to geometry through Reynolds Number.

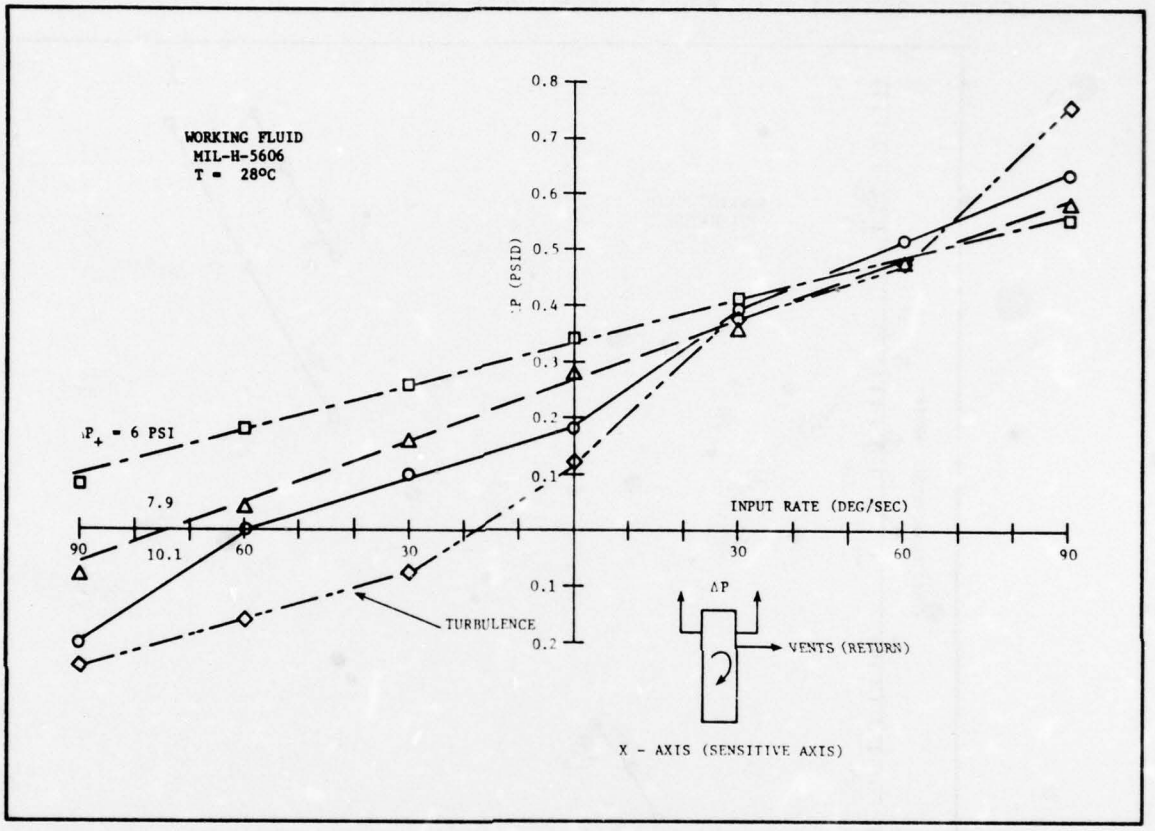

Figure 5-3. Laminar rate sensor output vs applied rate

Ideally, the jet is completely isolated from the sensor's surrounding structure during its passage from the power nozzle to the receiver; however, the jet is submerged in a field of solid body rotating fluid. This effect reduces the lateral displacement of the jet relative to the receiver structure. The LARS is appealing because it is far simpler than the FDSC and of lower output impedance than the VRS. The flow consumption and low pressure to achieve laminar flow leads to far less power

consumption than either the VRS or the FDSC. Figure 5-4 shows the relative power consumption of each of the three sensors.

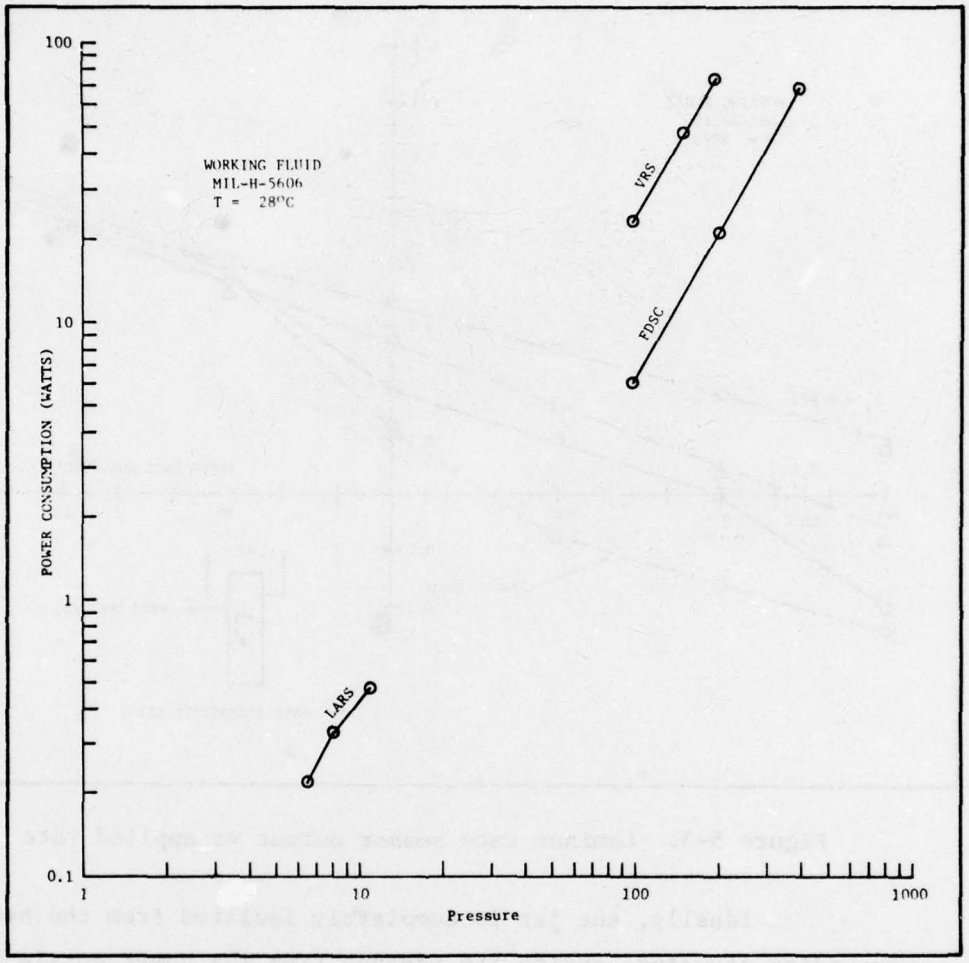

Figure 5-4. Power consumption as function of supply pressure

Reference 3 describes early research on the LARS for pneumatic applications, and it served as the basis for the design of the sensor which was tested under the program reported herein. That reference also showed that the null shift and temperature sensitivity of the LARS were high. It

---

[3] Young, R., "Feasibility Investigation Of A Laminar Angular Rate Sensor (LARS)", prepared under Contract No. N00018-72-C-0231, 1973.

can be expected that temperature and pressure fluctuations will be even more severe for the hydraulic sensor.

Figure 5-5a,b shows the effect of supply pressure and temperature variations on null shift as measured in this program.

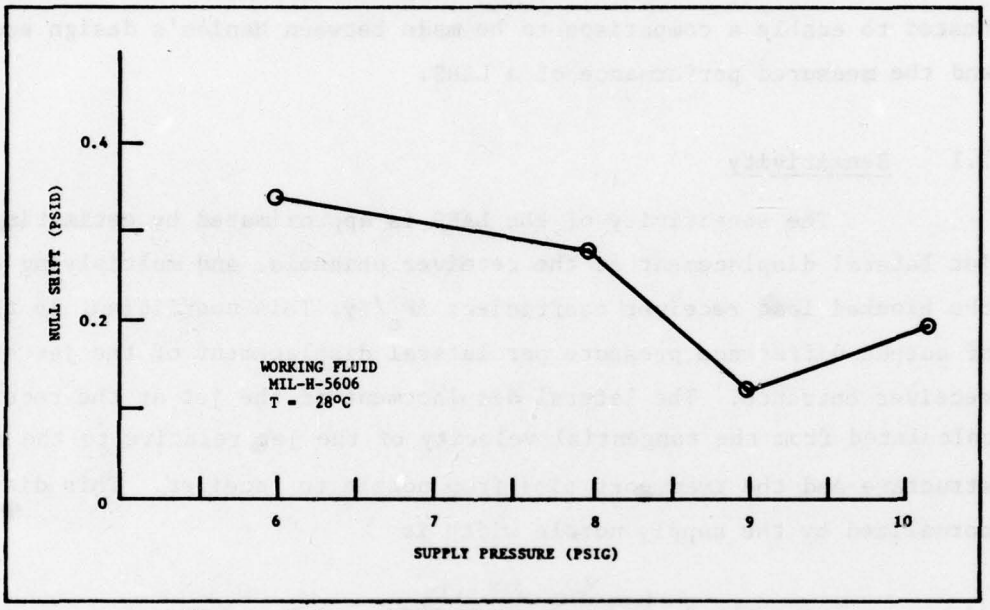

Figure 5-5a. Null shift with supply pressure

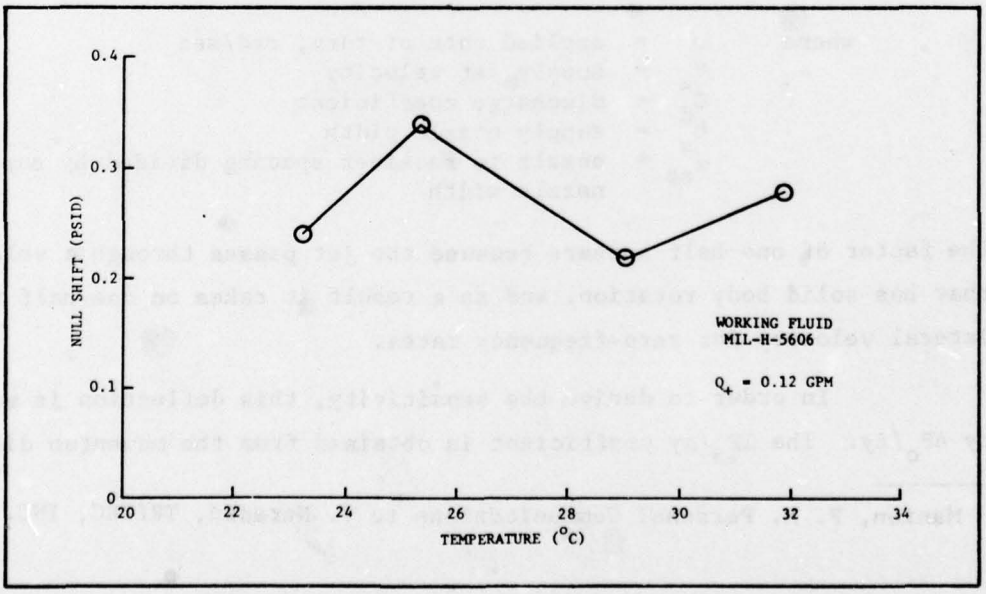

Figure 5-5b. Null shift with temperature

In an unpublished paper[7], Manion has developed engineering design equations for the LARS so that the designer can determine the interdependency of bandwidth, sensitivity, flow consumption, and the maximum rate that can be sensed by this device, and be able to make the design tradeoffs for a given application. In the following sections of this report, these equations will be derived and will be applied for the geometry of the unit tested to enable a comparison to be made between Manion's design equations and the measured performance of a LARS.

5.1 Sensitivity

The sensitivity of the LARS is approximated by estimating the jet lateral displacement at the receiver channels, and multiplying this by the blocked load receiver coefficient $\Delta P_o/\Delta y$. This coefficient is the change of output difference pressure per lateral displacement of the jet at the receiver entrance. The lateral displacement of the jet at the receiver is calculated from the tangential velocity of the jet relative to the receiver structure and the transport time from nozzle to receiver. This displacement normalized by the supply nozzle width is

$$\Delta y = \frac{1}{2} \frac{X_{sp}\,\omega\,(X_{sp} b_s)}{C_d V_s} \tag{18}$$

where
- ω = applied rate of turn, rad/sec
- V_s = supply jet velocity
- C_d = discharge coefficient
- b_s = supply nozzle width
- x_{sp} = nozzle to receiver spacing divided by supply nozzle width

The factor of one-half appears because the jet passes through a velocity field that has solid body rotation, and as a result it takes on one-half the receiver lateral velocity for zero-frequency rates.

In order to derive the sensitivity, this deflection is multiplied by $\Delta P_o/\Delta y$. The $\Delta P_o/\Delta y$ coefficient is obtained from the momentum difference in

[7] Manion, F. M. Personal Communications to V. Neradka, TRITEC, INC. 1978.

the output receivers per lateral displacement of the jet. In the analysis of laminar jet amplifiers, reference 8, this quotient is found to be

$$\frac{\Delta P_o}{\Delta Y} = \left(C_\theta\right)\left(1 - \frac{8x}{C_\theta N_R \sigma^2}\right)\left(1 - \frac{1.1\, B_{sp}}{\sqrt{C_d N_R \frac{B_{sp}}{2}}}\right)\frac{4P_s}{B_o\, b_s} \qquad (19)$$

where
- C_θ = jet momentum flux discharge coefficient, $1.32C_d^2$
- C_d = discharge coefficient
- σ = aspect ratio, nozzle height divided by width
- N_R = Reynolds Number $V_s b_s/\nu$
- B_{sp} = splitter/diameter divided by b_s
- P_s^o = output/receiver width divided by b_s
- supply pressure

The three terms in parenthesis account for momentum losses from the nozzle, along the surface plates, and around the splitter respectively. Development of equation 19 is given in reference 8, and using this expression, the sensitivity of the LARS can be defined as

$$S = \frac{b_s x}{2C_d V_s}\left(\frac{x}{B_o}\right)\left(\frac{4P_s}{57.3}\right)\left[C_\theta\left(1 - \frac{8x}{C_\theta N_R \sigma^2}\right)\left(1 - \frac{1.1\, B_{sp}}{\sqrt{C_d N_R \frac{B_{sp}}{2}}}\right)\right] \qquad (20)$$

Defining a loss coefficient, K_ℓ as

$$K_\ell = C_\theta\left(1 - \frac{8x}{C_d N_R \sigma^2}\right)\left(1 - \frac{1.1\, B_{sp}}{\sqrt{C_d N_R \frac{B_{sp}}{2}}}\right) \qquad (21)$$

the sensitivity, equation (20), becomes

$$S = \frac{b_s}{2V_s}\left(\frac{x^2}{B_o}\right)\left(\frac{4P_s}{57.3}\right)\frac{K_\ell}{C_d} \qquad (22)$$

Replacing P_s with the equivalent jet velocity, and introducing the Reynolds Number ($N_R = \rho V_s b_s/\mu$) in equation 22 , the sensitivity becomes

$$S = \frac{x^2}{B_o} N_R \frac{\mu}{57.3}\frac{K_\ell}{C_d} \qquad (23)$$

---

[8] Manion, F.M. and Drzewiecki, T.M., "Analytical Design of Laminar Proportional Amplifier", Volume I, Fluidic State-Of-The-Art Symposium, October 1974, page 149.

Studies at HDL have indicated that there is a relationship between the maximum Reynolds Number and the nozzle-to-receiver distance for transition to turbulence in the jet stream before the receiver. Laminar boundary layer theory suggests that N_R varies inversely with the distance between power nozzle exit and the receiver entrance. Therefore, in order to approximate the relationship between the splitter, it is assumed that

$$N_c = \frac{\overline{N}_R \, 8}{x_{sp}} \tag{24}$$

where $\overline{N}_R$ is the maximum Reynolds Number for a fluidic amplifer with a geometrical configuration of $x_{sp} = 8$. This expression reduces the maximum Reynolds Number as the splitter is removed further downstream. Although it is only an approximation, it has merit and aids the designer in the sensor tradeoffs. In deriving the foregoing equation for the sensitivity, it is assumed that there is no effect from bias flow or entrainment flow differences as the jet is displaced into the control nozzle region. It should be noted that this assumption is invalid for sensors that have control regions similar to HDL-LPA Model 2-2B (4 nozzle width control units) such is shown in Figure 5-6. Control volume analysis similar to that described in Reference 8 shows that the sensitivity depends on x_{sp}^2 only when there are no pressure effects in the control nozzle region. When there are pressure effects in the control region, x_{sp}^2 in the sensitivity equation is replaced by

$$B_c^2\left(1 - \frac{B_c^2}{4C_c}\left(\frac{R_v R_c}{P_s + R_c}\right)\left(\frac{P_j - P_v}{P_s - P_v}\right) - a_1\left(\frac{2x}{B_c} - 1\right) + \left(x - B_c\right)^2\right) \tag{25}$$

where
- B_c is a control nozzle width divided by b_s
- R_v^c is the vent resistance, normalized by R_s, (i.e., P_s/Q_s)
- R_c is the control resistance normalized by the supply resistance P_s/Q_s
- $P_j - P_v$ is the pressure difference between the control region and the vent (These pressures are normalized by P_s)
- a_1 is the difference in entrainment flow coefficent

[8] Manion, F.M. and Drzewiecki, T.M., "Analytical Design of Laminar Proportional Amplifier", Volume I, Fluidic State-Of-The-Art Symposium, October 1974, page 149.

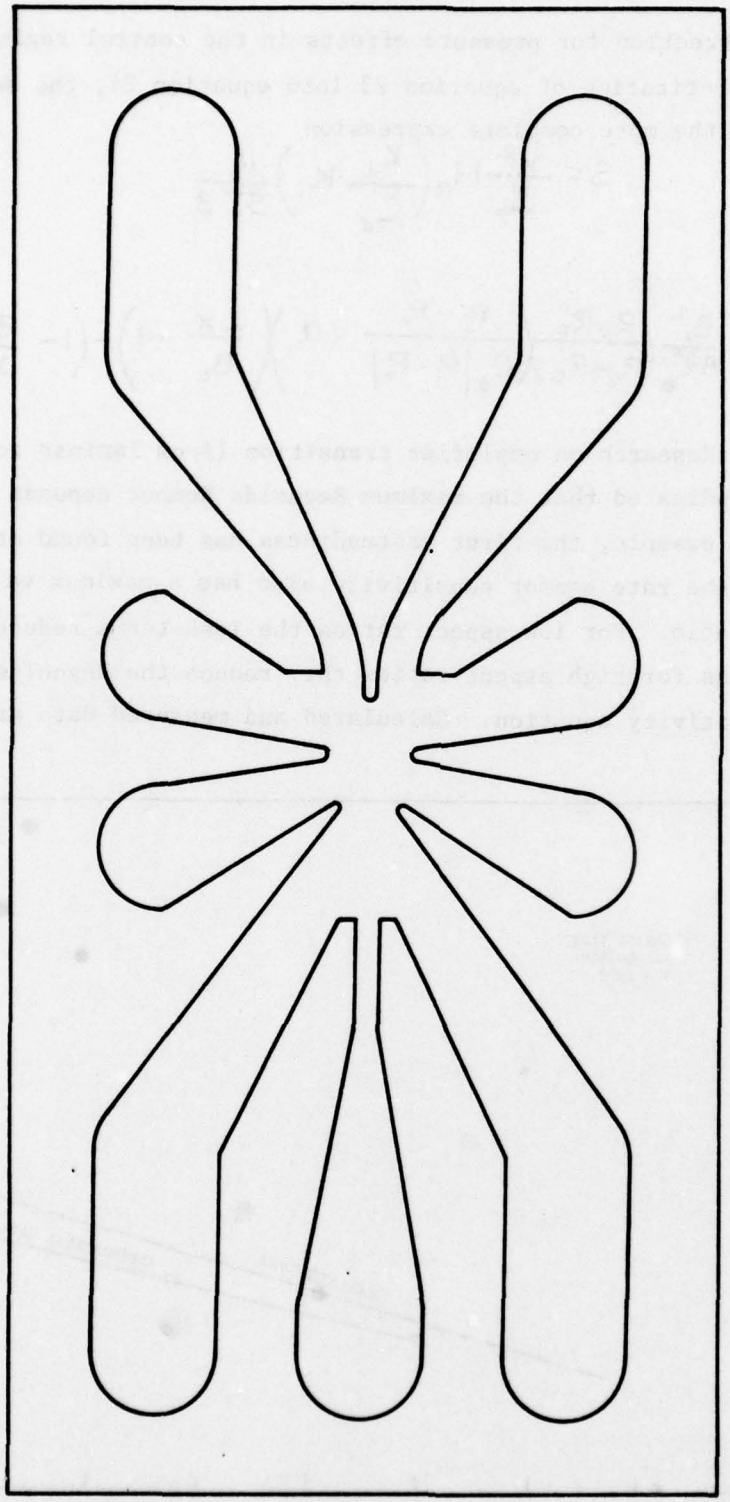

Figure 5-6. HDL-LPA Model 2-2B Silhouette

With the correction for pressure effects in the control region, obtained from the substitution of equation 23 into equation 24, the sensitivity is replaced by the more complete expression

$$S = \frac{X^2}{B_o} N_R \left(\frac{K_1}{C_d} K_i \right) \frac{\mu}{57.3} \qquad (26)$$

$$K_i = \left(\frac{B_c}{X} \right)^2 \left(1 - \frac{B_c^2}{4 C_d} \left(\frac{R_v R_c}{R_v + R_c} \left(\frac{P_j - P_v}{C_d |P_j - P_v|} + a_1 \right) \left(\frac{2X}{B_c} - 1 \right) + \left(1 - \frac{B_c}{X} \right)^2 \right) \right) \qquad (27)$$

Research on amplifier transition (from laminar to turbulent flow) has indicated that the maximum Reynolds Number depends on aspect ratio ; for example, the first unsteadiness has been found at $N_R \sigma = 1400$. Therefore, the rate sensor sensitivity also has a maximum value that depends on aspect ratio. For low aspect ratios the loss terms reduce the sensitivity; whereas for high aspect ratios they reduce the Reynolds Number term in the sensitivity equation. Calculated and measured data are shown in Figure 5-7.

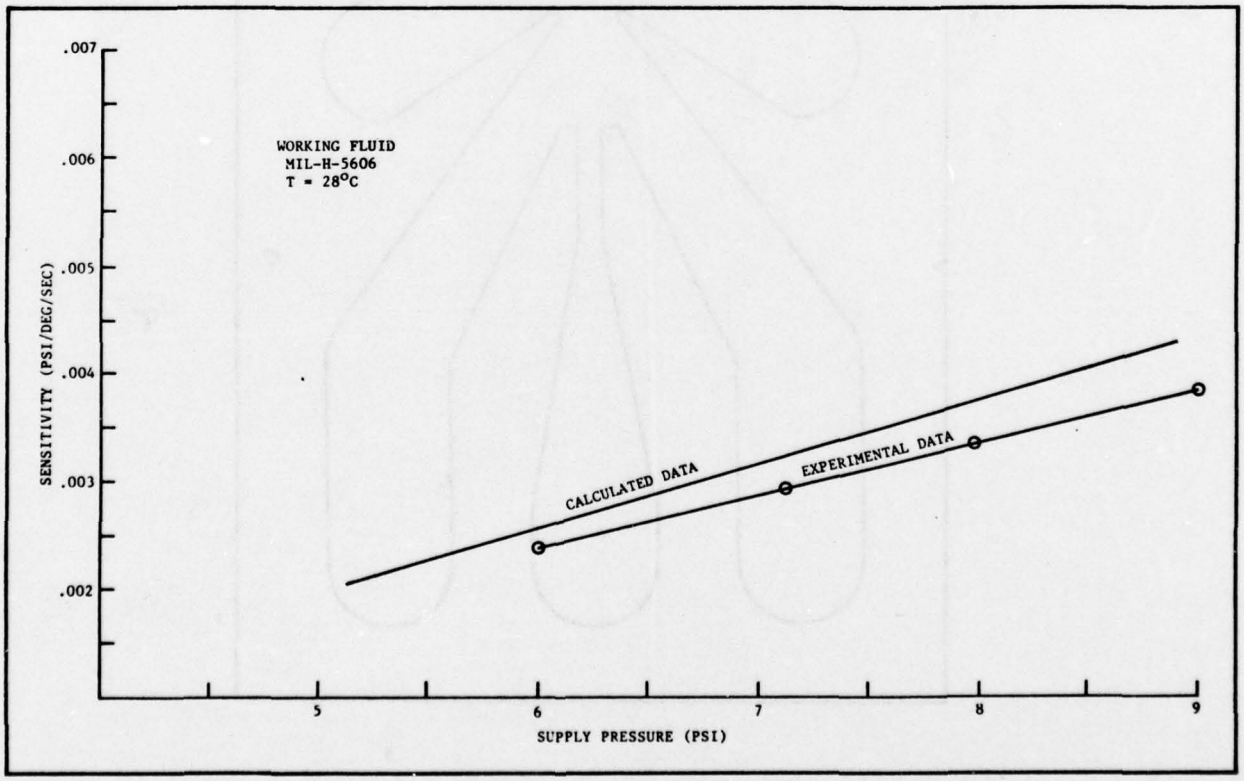

Figure 5-7. Comparison of LARS calculated and experimental data

5.2 Bandwidth

The bandwidth of the sensor is defined as the frequency of 90^{o} phase lag due to jet transport when the input and output impedances can either be isolated from the deflecting jet stream, or have negligible phase lag in this frequency range. The transport lag is calculated from average stream velocity and the spacing from the supply nozzle exit to the receiver input. The frequency at which 90^{o} phase lag occurs is then given by

$$f = \frac{c_d V_s}{8 x_{sp} b_s} \tag{28}$$

where c_d = discharge coefficient
V_s = supply velocity $\sqrt{2 P_+ / \rho}$
b_s = supply nozzle width
x_{sp} = nozzle to receiver spacing divided by the supply nozzle width, b_s

For the particular LARS which was tested, the calculated values of bandwidth as a function of supply pressure are as shown in Figure 5-8 .

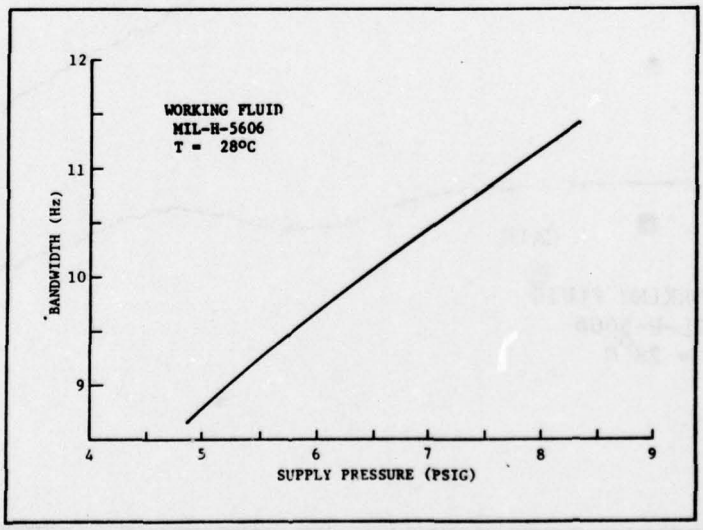

Figure 5-8. LARS bandwidth vs supply pressure

The attempt to verify this prediction of bandwidth experimentally was only partially successful. The data showed an experimental bandwidth of 10.5 Hz. However, the data showed somewhat of a lead function characteristic in both phase and amplitude ratio, which is totally unexpected for the type of element under test. Unfortunately, under the constraints of the program status, extraneous factors such as instrumentation dynamics could not be adequately tracked down. Figure 5-9 shows, as an alternative, data which has been provided by HDL* for completeness of presentation herein. This data shows a bandwidth of 12 Hz and a (nearly) constant amplitude ratio such as is expected.

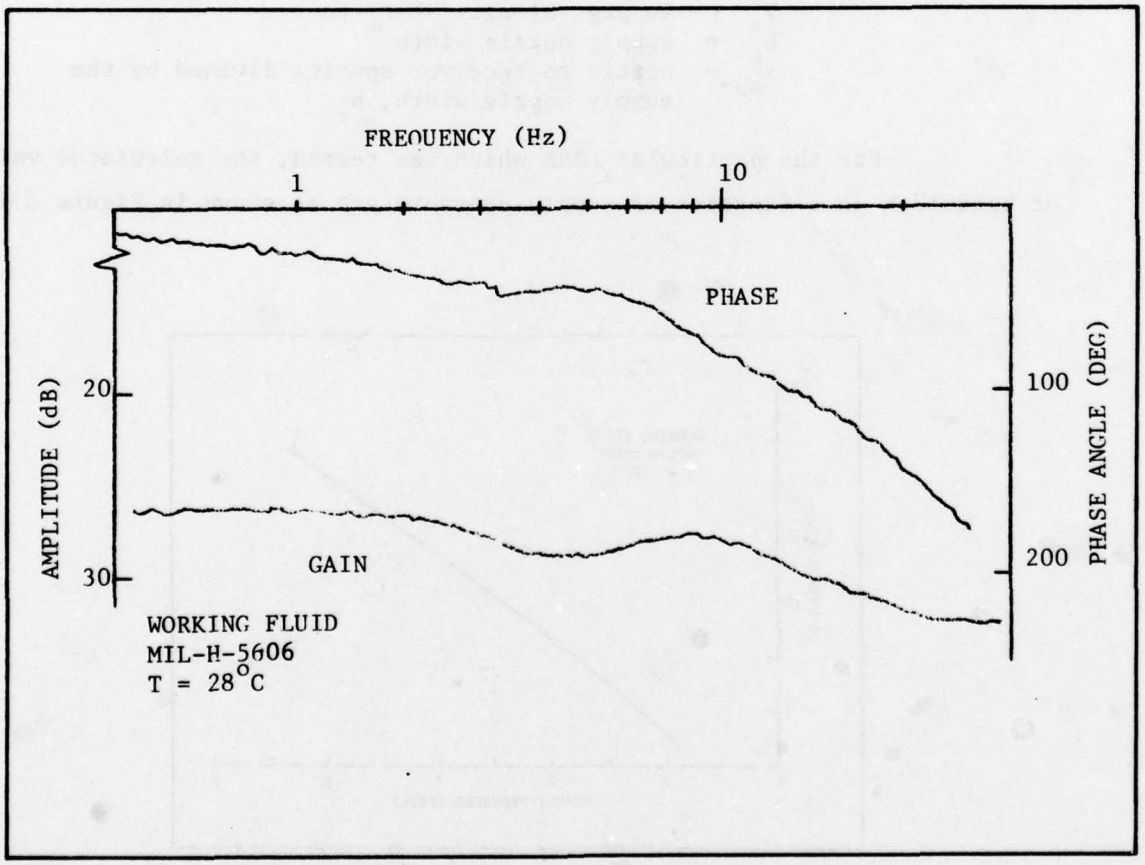

Figure 5-9. LARS gain and phase as a function of frequency

* Personal communications between T. Drzeweicki and V. Neradka, TRITEC, 1978.

5.3 Maximum Rate Of The Sensor

The LARS maximum rate capacity can be estimated by assuming that the maximum rate signal deflects the jet enough to center it in the receiver output.

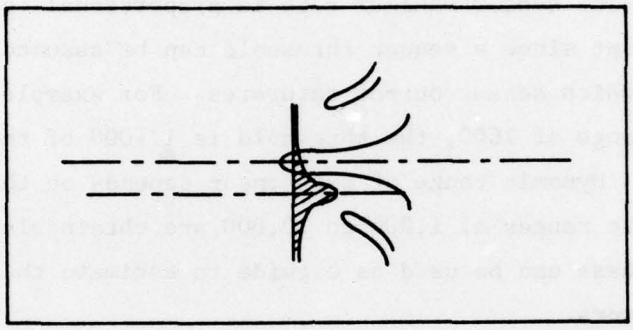

Figure 5-10. Jet position under condition of maximum allowable jet deflection

This, of course, is only an estimate, for if the jet were much narrower than the receiver, a deflection approximately one-half of the jet would result in a maximum signal; but receivers are not designed this wide because they would have poor pressure recovery.

Referring to the equation for the displacement of the jet and substituting $B_o/2$ for the jet displacement and Δy, solving for maximum (or saturation) rate, $\dot{\theta}_m$

$$\dot{\theta}_m = \frac{0.5 B_o}{2X} \frac{C_d V_s}{X_{sp} b_s} \tag{29}$$

$$\dot{\theta}_m = \frac{B_o f}{X} \tag{30}$$

where f is the bandwidth as previously defined in equation 28.

For the unit which was tested, the maximum applied rate which can be sensed is 435 degrees/second at 6 psi supply pressure. As could be expected from the data of Reference 3, this figure far exceeds that which was measured. The limitation in rate is one of experimental equipment rather than capability of the LARS.

The sensor maximum rate is proportional to its bandwidth. This is significant since a sensor threshold can be assumed to depend on the value of rate at which sensor output saturates. For example, if the sensor has a dynamic range of 1000, the threshold is 1/1000 of the rate that saturates the sensor. Dynamic range of the sensor depends on the flow field and typical dynamic ranges of 1,000 to 10,000 are obtainable with laminar flow devices. These can be used as a guide to estimate the threshold/bandwidth of LARS sensors.

5.4 Output Impedance

Another important parameter in the characterization of a sensor is its output impedance or resistance to a zero-frequency signal. The laminar amplifers and sensors typically have an output resistance of about one-half the supply resistance. The supply resistance is defined as

$$R_s = \frac{P_s}{Q_s} = \frac{\rho V_s}{2C_d b_s^2 \sigma} \tag{31}$$

Once again, redefining in terms of the Reynolds Number

$$R_s = \frac{N_R}{2C_d \sigma} \frac{\mu}{b_s} \tag{32}$$

Therefore, the output resistance is approximately

$$R_o = \frac{N_R}{4C_d \sigma} \frac{\mu}{b_s} \tag{33}$$

The output impedance is essentially this output resistance over the frequency range of interest; namely low frequency.

---

[3] Young, R., "Feasibility Investigation Of A Laminar Angular Rate Sensor (LARS)", prepared under Contract No. N00018-72-C-0231, 1973.

5.5 Threshold

The test data leading to the determination of threshold which TRITEC recorded provided to be inconclusive as a result of instrumentation difficulties. Data provided by HDL* indicate a threshold rate of 0.167 deg/sec.

5.6 Cross-Axis Sensitivity

The cross-axis sensitivity of the LARS is shown in Figure 5-12 for the remaining two mutually perpendicular axes. The cross-axis sensitivity is less for the LARS than for the FDSC.

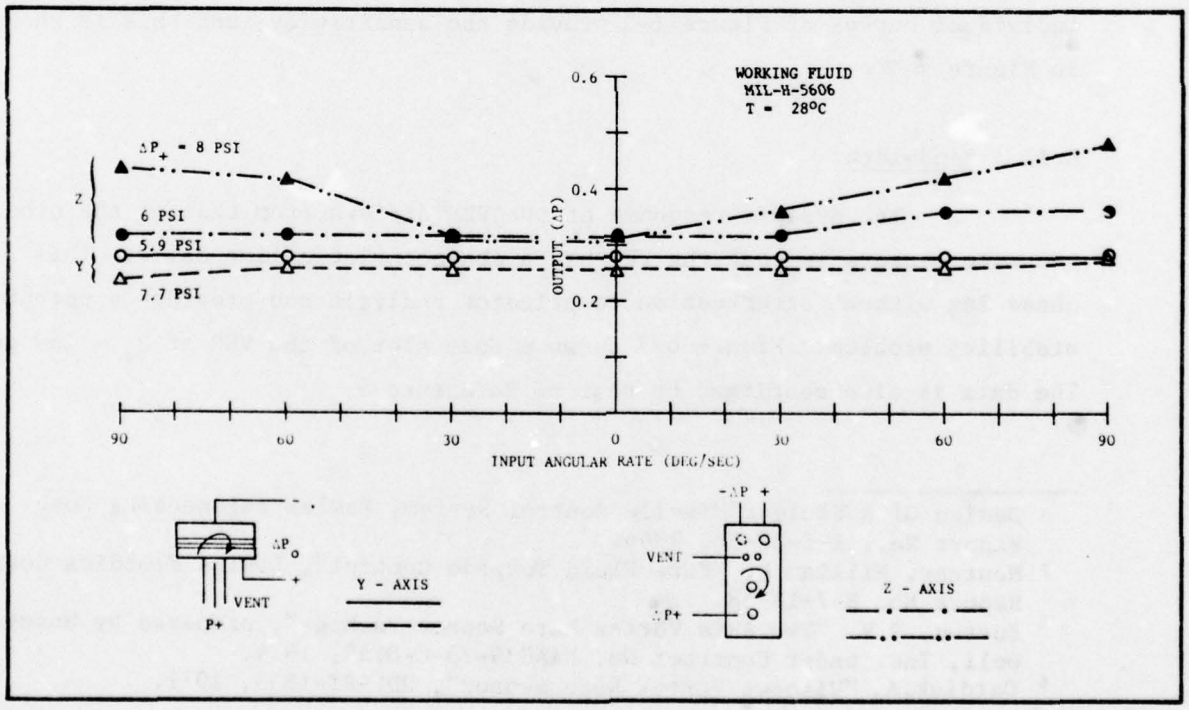

Figure 5-11. Cross axis sensitivities for LARS

* Unpublished data provided courtesy of T. Drzeweicki, HDL

6.0 VORTEX RATE SENSOR ANALYSIS

The VRS is the earliest of the rate sensing devices in the field of fluidics. Since that time it has been applied to numerous systems.[1,2,5] The vortex flow model has been theorized and verified experimentally in rigorous detail.[6]

6.1 Sensitivity

This sensor was tested over much the same range as the FDSC except that flow limitations of the test facility prohibited testing at the highest pressure of the FDSC tests. The characteristic output signal seen in Figure 6-1 indicates good linearity and range. The slopes of the individual curves of Figure 6-1 provide the sensitivity, and this is shown in Figure 6-2 .

6.2 Bandwidth

The dynamic response of the VRS differs from that of the other two rate sensors in that the VRS has a characteristic time delay. This phase lag without attentuation complicates analysis and provides a potential stability problem. Figure 6-3 shows a Bode plot of the VRS at P_+ = 150 psig. The data is also confirmed by that of Reference 5.

---

1 Design Of A Fluidic Missile Control System, Bowles Engineering Corp. Report No.. R-5-20-66, 1966.

2 Mentzer, William R. "Pure Fluid Torpedo Control", Bowles Fluidics Corp. Report No. R-7-18-68.

5 Burton, R.V. "Two Axis Vortex Rate Sensor Package", prepared by Honeywell, Inc. under Contract No. DAAG39-/3-C-0159, 1974.

6 Ostdiek,A. "Viscous Vortex Rate Sensor", HDL-RT-1555, 1971.

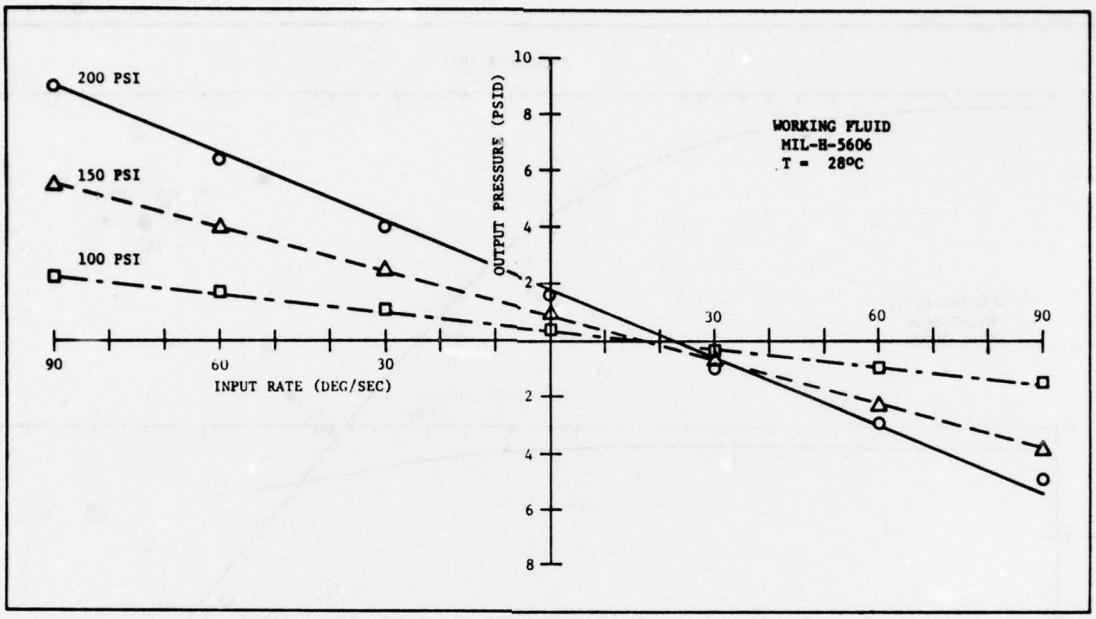

Figure 6-1. VRS output as function of applied rate

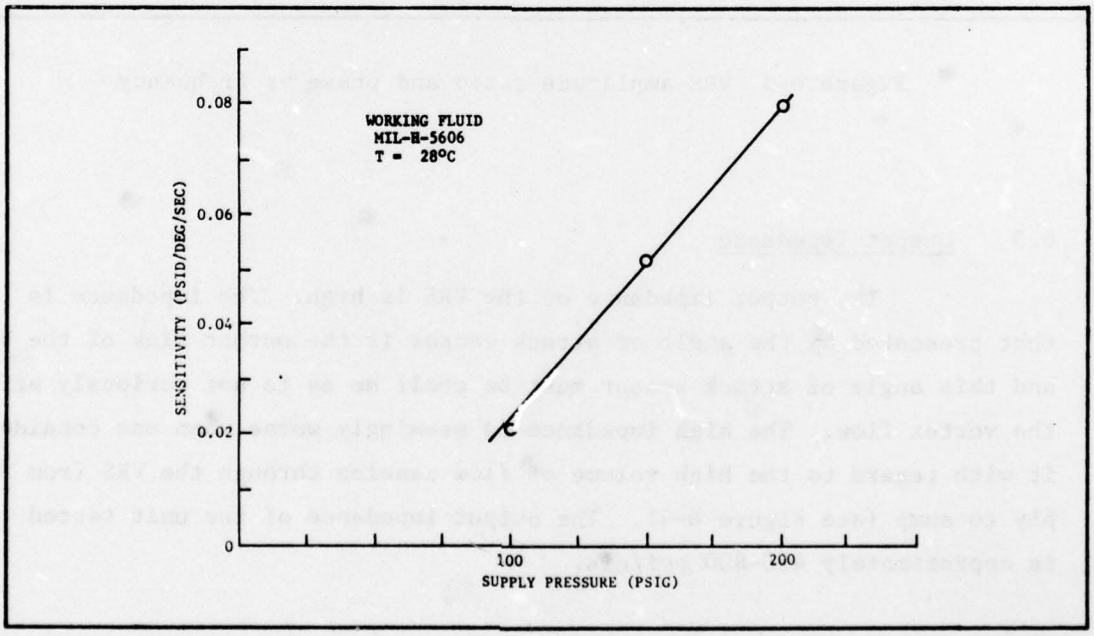

Figure 6-2. Sensitivity of VRS with supply pressure

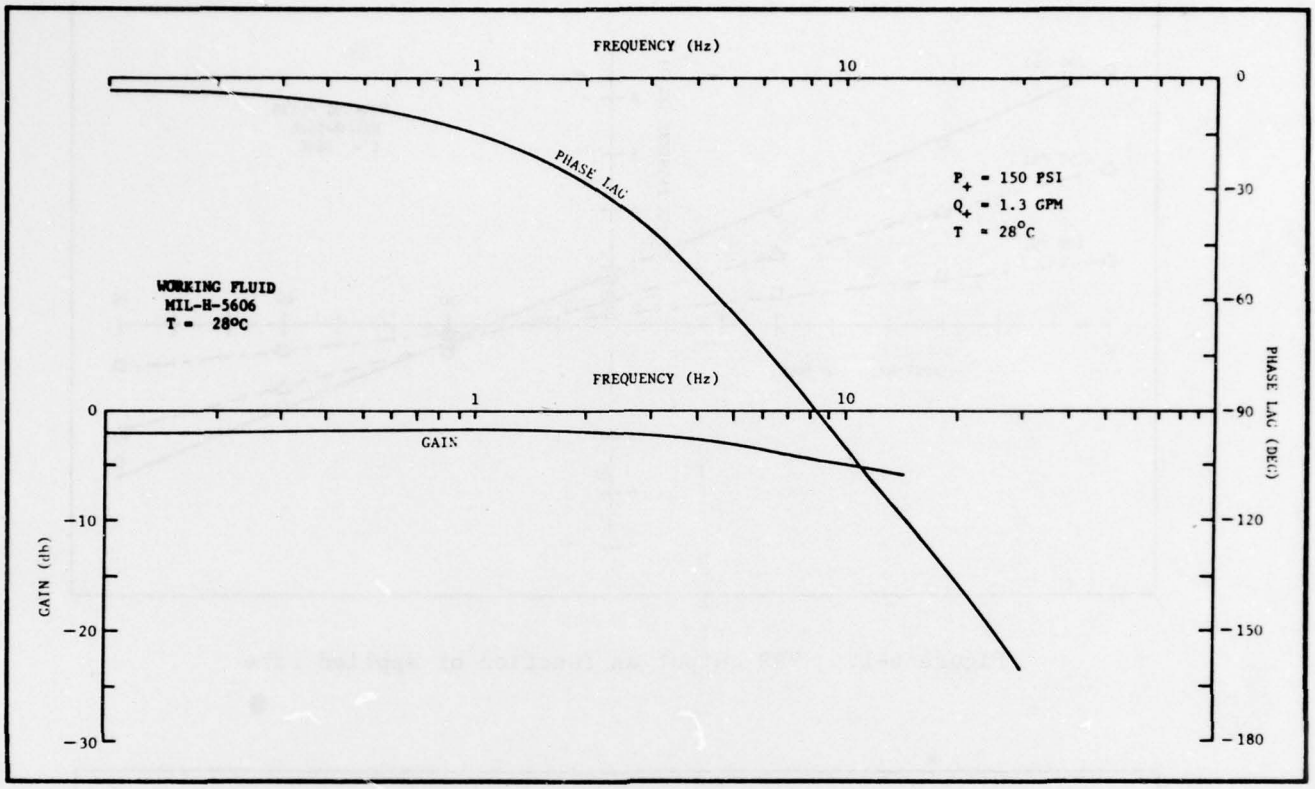

Figure 6-3 VRS amplitude ratio and phase vs frequency

6.3 Output Impedance

The output impedance of the VRS is high. The impedance is that presented by the angle of attack sensor is the output sink of the VRS, and this angle of attack sensor must be small so as to not seriously affect the vortex flow. The high impedance is seemingly worse when one considers it with regard to the high volume of flow passing through the VRS from supply to sump (see Figure 6-4). The output impedance of the unit tested is approximately 400-800 psi/cis.

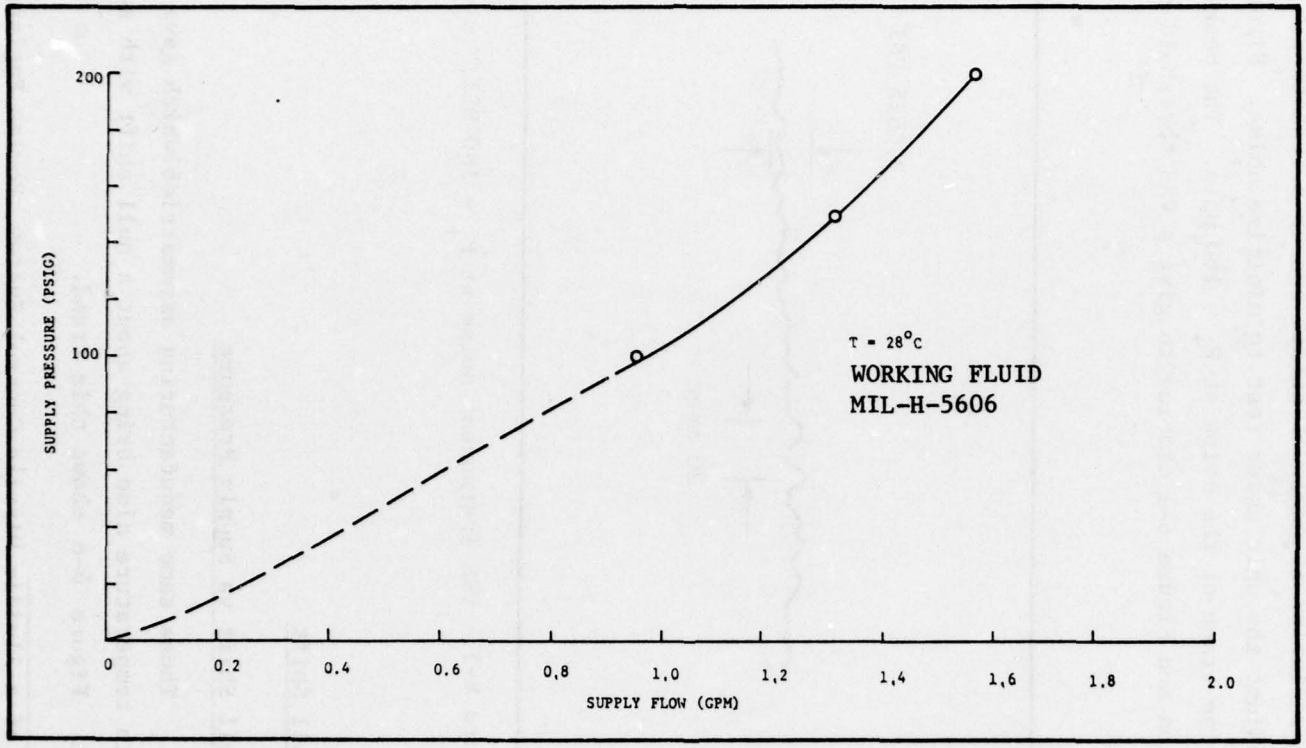

Figure 6-4. Supply pressure-flow characteristic

6.4 Threshold

Reference 1 shows that the noise of the VRS can vary considerably with variation of angle of attack sensor orientation. No attempt was made to adjust the unit under test to minimize noise. Figure 6-5 shows the oscilloscope trace of the noise at P_+ = 180 psig. The peak-to-peak pressure fluctuation and Figure 6-1 combine to give a VRS threshold of 0.25 deg/sec.

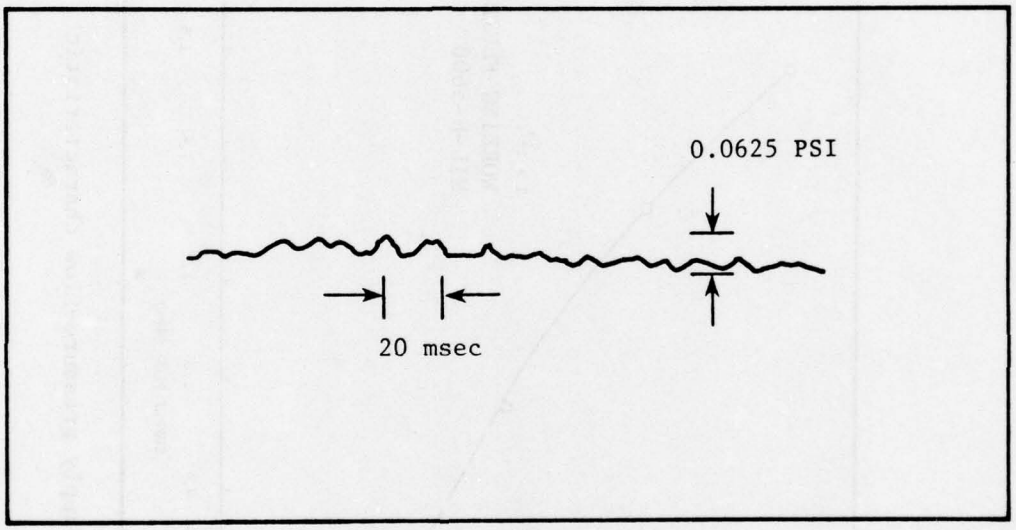

Figure 6-5. VRS instrument noise at P_+ = 180 PSI, ω = 0

6.5 Null Shift

6.5.1 Null Shift vs Supply Pressure

Those same manufacturing asymmetries which gave rise to null shift with temperature also bring about a null shift with supply pressure variation. Figure 6-6 shows this trend.

[1] Design of a Fluidic Missile Control System, Bowles Engineering Corp. Report No. R-5-20-66, 1966.

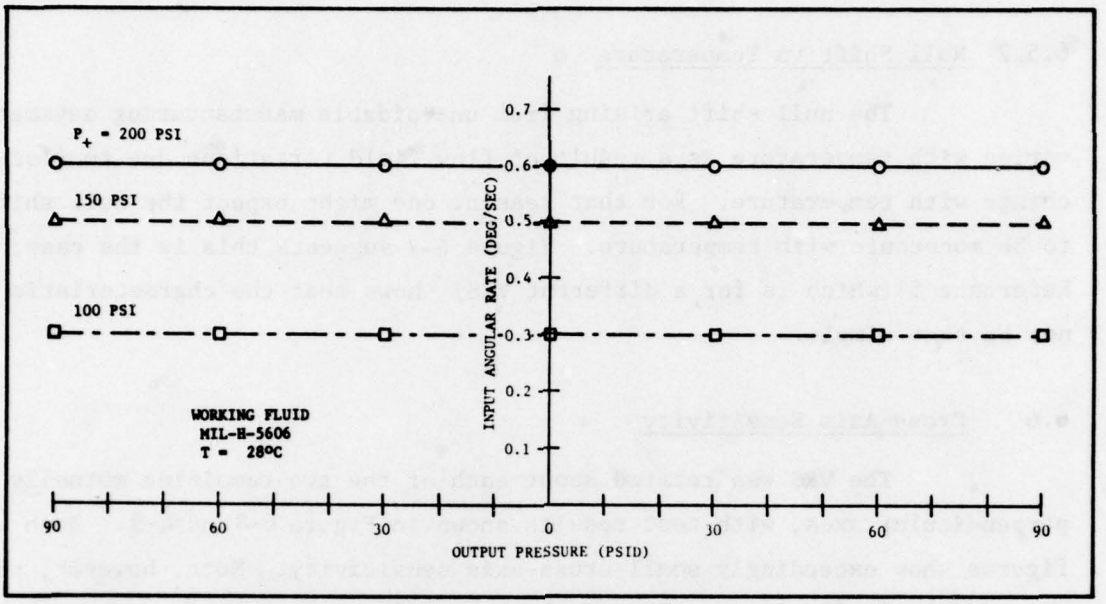

Figure 6-6. Null shift vs supply pressure

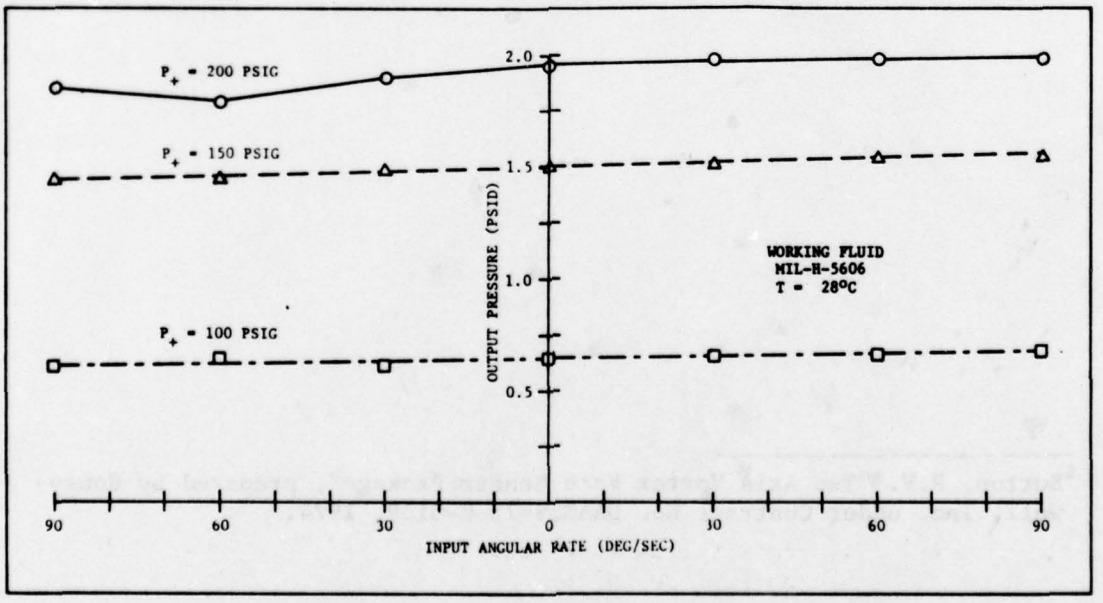

Figure 6-7. Null shift vs temperature

6.5.2 Null Shift vs Temperature

The null shift arising from unavoidable manufacturing asymmetries varies with temperature as a result of flow field variations due to viscosity change with temperature. For that reason, one might expect the null shift to be monotonic with temperature. Figure 6-7 suggests this is the case, but Reference 5 (which is for a different VRS) shows that the characteristic may not be that simple.

6.6 Cross-Axis Sensitivity

The VRS was rotated about each of the two remaining mutually perpendicular axes, with test results shown in Figure 6-8 and 6-9. Both figures show exceedingly small cross-axis sensitivity. Note, however, that they differ in ΔP offset. This could be attributed to the fact that the angle of attack sensor is not axisymmetic and the vortex effluxing through the sink is affected by fluid weight.

---

[5]Burton, R.V. "Two Axis Vortex Rate Sensor Package", prepared by Honeywell, Inc. under Contract No. DAAG39-73-C-0159, 1974.

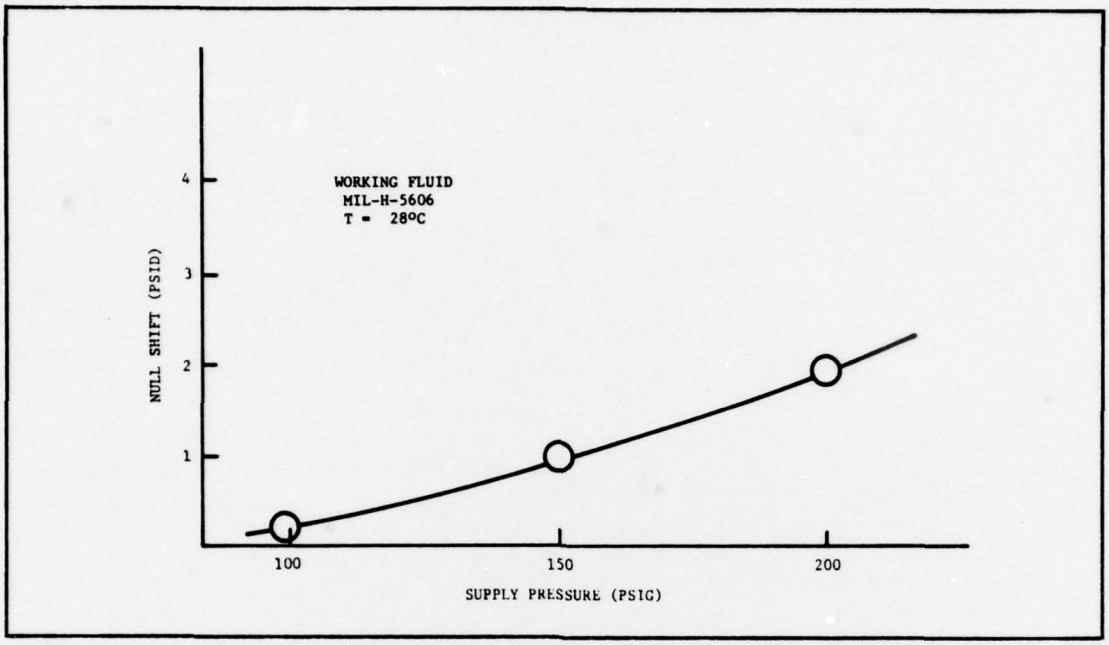

Figure 6-8. Cross-axis sensitivity

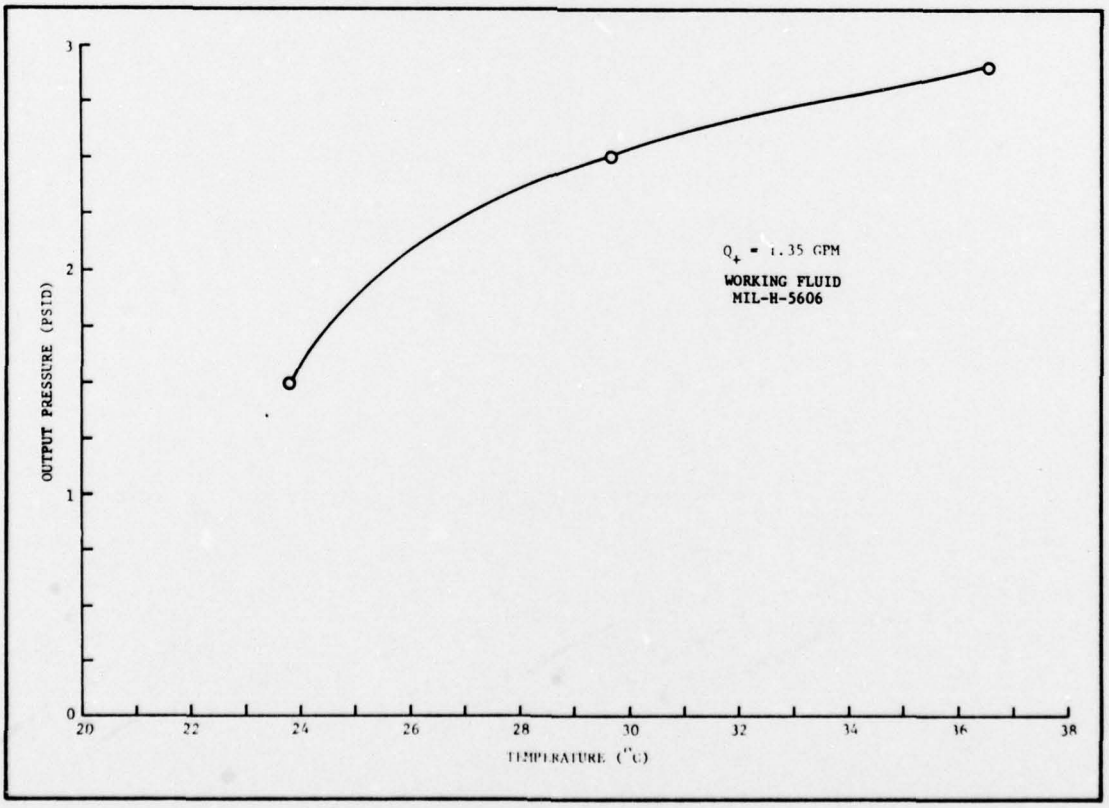

Figure 6-9. Cross-axis sensitivity

APPENDIX A

SENSITIVITY OPTIMIZATION ANALYSIS

OF

FLUIDISC BRIDGE CIRCUIT

INTRODUCTION

Under contract DAAG39-77-C-0173 of the Harry Diamond Laboratories, TRITEC, INC. is pursuing an investigation to determine the baseline performance level of three rate gyros, namely the Fluidisc, the Vortex Rate Sensor, and the Laminar Jet Rate Sensor. During a preliminary analysis of the Fluidisc, it appears that physical parameters which are not optimum were used in the previous tests. Reluctant to perform any tests if this turns out to be the case, TRITEC has performed an analysis on the relevant portion of the sensor output (i.e. the resistive bridge network) for HDL review and discussion in order that the Government's objectives best be met.

TECHNICAL DISCUSSION

Figure A-1 shows the Fluidisc gyro schematic diagram.

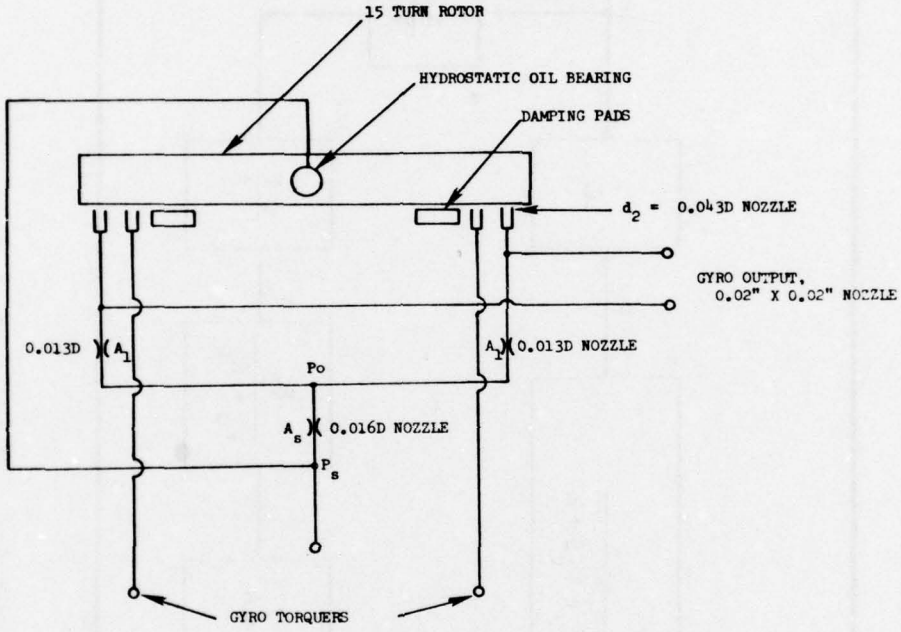

Shown on the figure are two sets of flapper nozzles, one for torque feedback to restrain the seismic mass and one to provide an external input signal to the gyro. Figure A-2 shows their functional interrelationship in the simplest of terms.

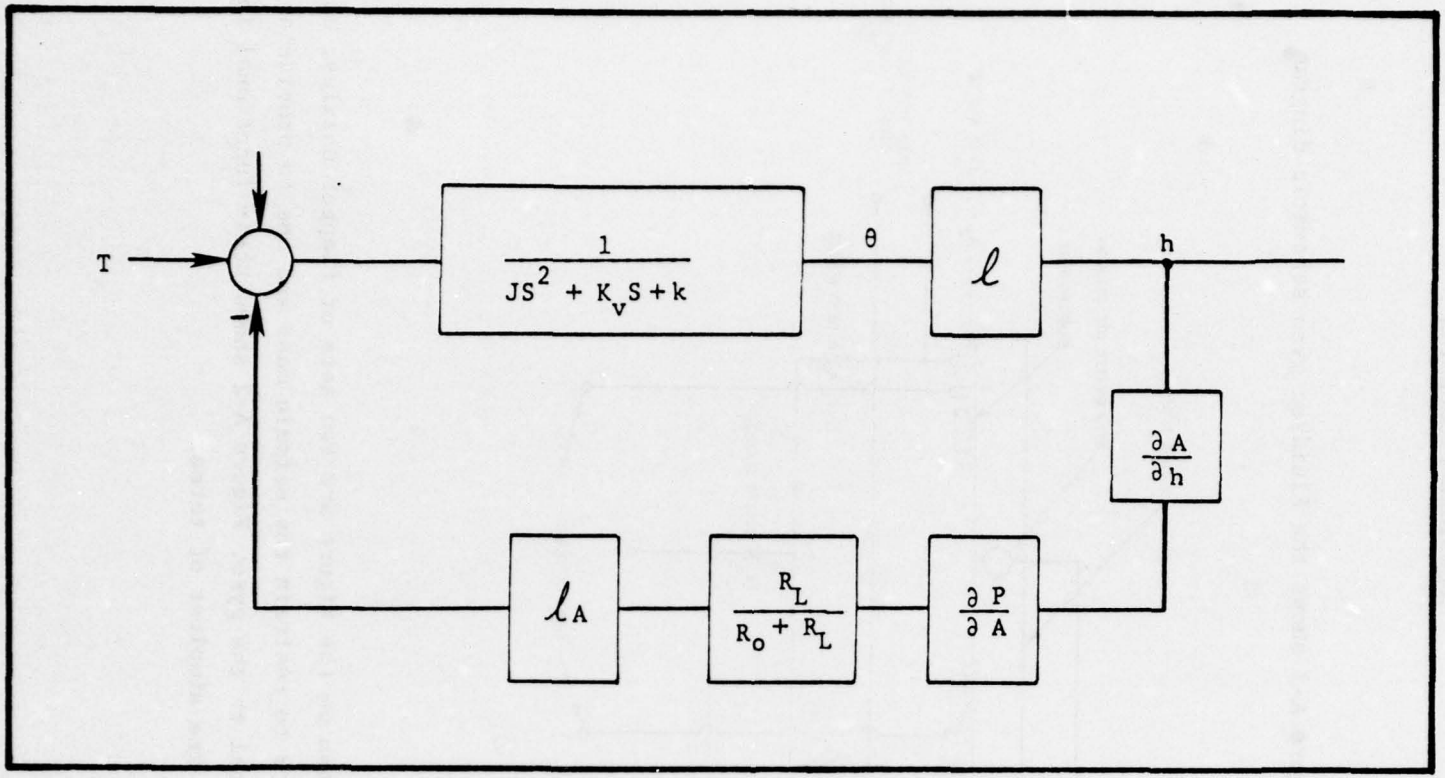

Figure A-2. Fluidisc block diagram

From the viewpoint of the sensor portion of the schematic, the resistive bridge gain, $\partial P/\partial h$, is to be maximized.

The Fluidisc resistive bridge is shown in Figure A-3.

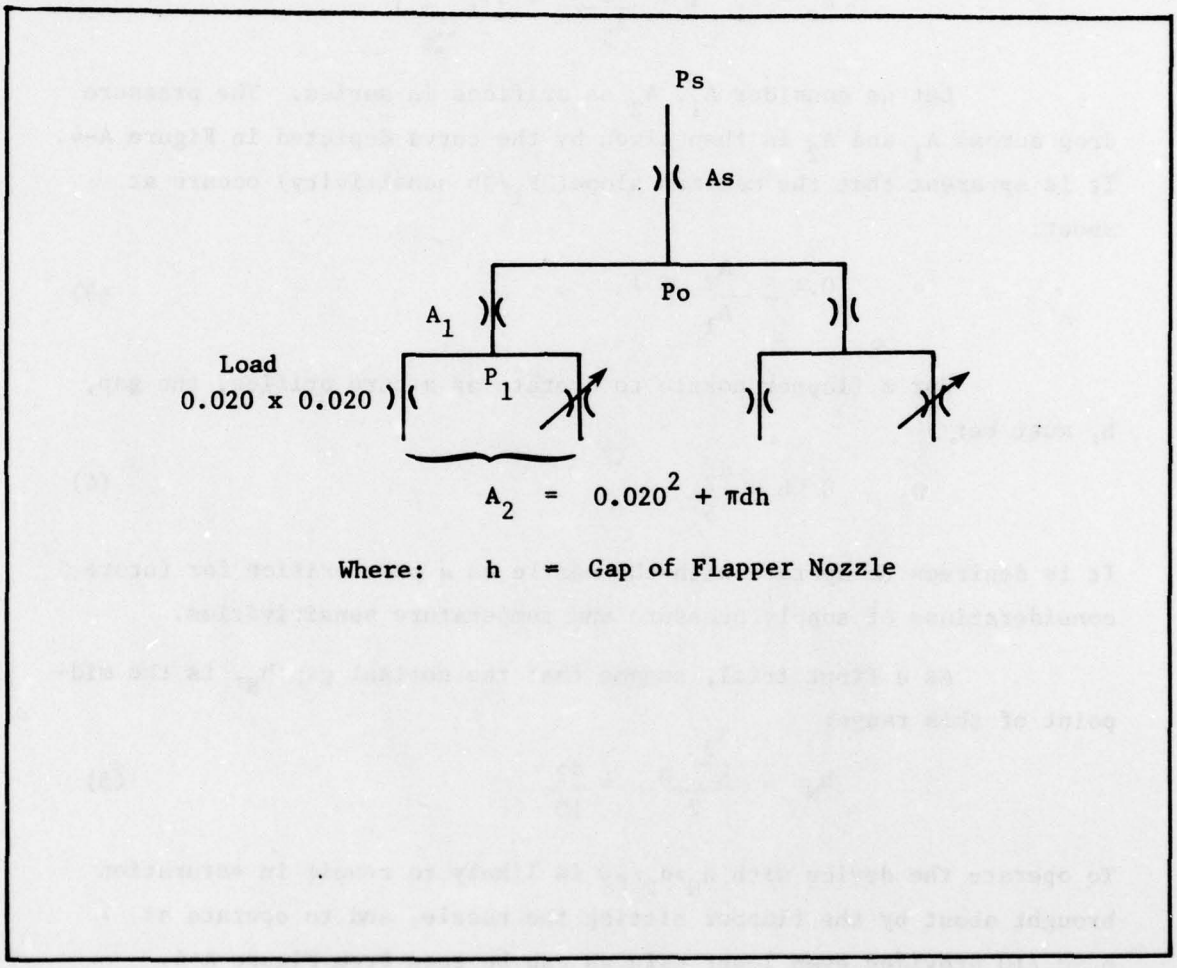

Figure A-3. Fluidisc resistive bridge

It can be shown that for the circuit in Figure A-3.

$$P_o = P_1\left[1 + \left(\frac{A_2}{A_1}\right)^2\right] \tag{1}$$

$$P_s = P_1\left[1 + \left(\frac{A_2}{A_1}\right)^2 + 4\left(\frac{A_2}{A_s}\right)^2\right] \tag{2}$$

Let us consider A_1, A_2 as orifices in series. The pressure drop across A_1 and A_2 is then given by the curve depicted in Figure A-4. It is apparent that the maximum slope($\partial P_1/\partial h$ sensitivity) occurs at about:

$$0.4 \leq \frac{A_2}{A_1} \leq 1 \tag{3}$$

For a flapper nozzle to operate as a pure orifice, the gap, h, must be:

$$0 < h \leq \frac{d_2}{5} \tag{4}$$

It is desirous to operate with the nozzle as a pure orifice for future considerations of supply pressure and temperature sensitivities.

As a first trial, assume that the nominal gap h_N, is the mid-point of this range:

$$h_N = \frac{\frac{d_2}{5} - 0}{2} = \frac{d_2}{10} \tag{5}$$

To operate the device with $h_N > d_2/10$ is likely to result in saturation brought about by the flapper hitting the nozzle, and to operate at $h_N > d_2/10$ provides even lower gain as can be seen from Figure A-4.

As was shown in Figure A-3

$$A_2 = 0.020^2 + \pi d_2 h \tag{6}$$

(It has been assumed that the load to be driven by the Fluidisc is a standard G.E. element of P_+ nozzle 0.020in. x 0.020 in.)

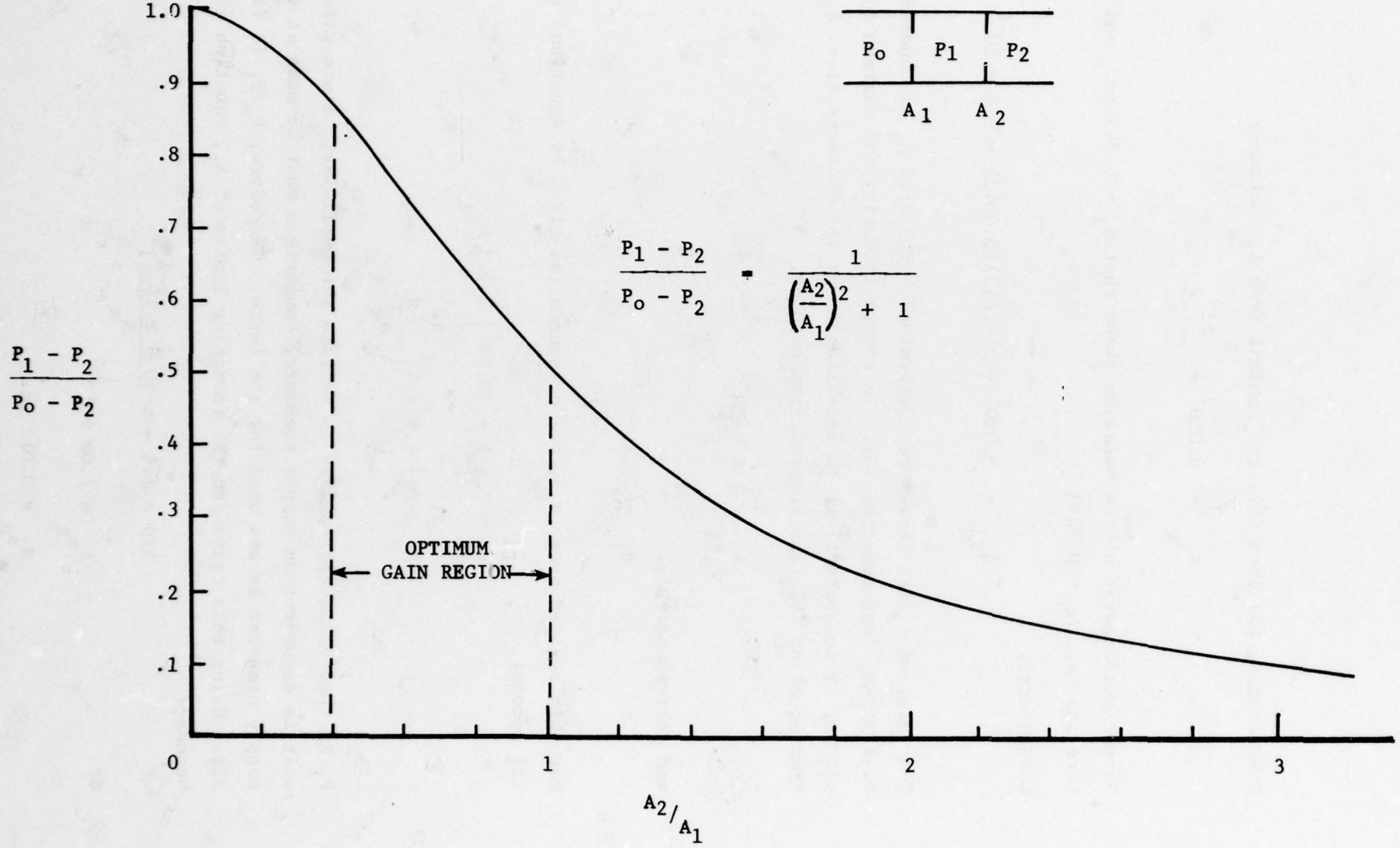

Figure A-4. Pressure drop across two orifices in series for incompressible flow

Substituting (5) into (6), the nominal area A_{2_N} becomes:

$$A_{2_N} = 0.020^2 + \frac{\pi d_2^2}{10} \tag{7}$$

Direct measurement of the hardware shows that $d_2 = 0.043$ in., and therefore the gap, $h_N = 0.0043$ in.

Consequently,

$$A_{2_N} = 0.020^2 + \pi(0.043)(0.0043) = 9.8 \times 10^{-4} \tag{8}$$

The value of A_2 is, therefore, determined. The area A_1 is bounded by $0.4A_1 < A_2 < A_1$ from equation (3). To ensure linearity and maximum design latitude, it is appropriate to establish A_1 at the midrange (i.e. $A_{2_N} = 0.7A_1$). From equation (8), the revised area becomes,

$$A_{1_R} = 1.4 \times 10^{-3}$$

and correspondingly,

$$d_{1_R} = 0.042$$

For this revised area, A_{1_R}, the pressures (as given by equations (1) and (2) become:

$$P_o = P_1\left[1 + (0.7)^2\right] \simeq 1.5\ P_1 \tag{9}$$

$$P_s \simeq P_1\left[1.5 + 4\left(\frac{A_{2_N}}{A_s}\right)_R\right] \tag{10}$$

P_1 is that value appropriate to operate the amplifier. Since gain of the unit is dependent on supply pressure, comparison must be made at the same supply pressure as was used for the tests. Therefore, P_s/P_1 is fixed at 329. Using this ratio and the foregoing limits of A_2, equation (10) becomes:

$$329 = 1.5 + 4\left(\frac{9.8 \times 10^{-4}}{A_s}\right)^2_R \tag{11}$$

or

$$A_{s_R} = 1.08 \times 10^{-4}$$

$$d_{s_R} = 0.012 \text{ in.}$$

These revised orifice diameters, which are expected to provide higher Fluidisc gain ($\partial P/\partial w$), are next compared with those values of diameter given by General Electric. Figure A-5 shows the resistance bridges in question, namely, the revised diameters.

The plot of P_1/P_s vs h is shown for both configurations in Figure A-6. The previous assumption regaring not having $h>d_2/5$ is further substantiated in that the slope, $d(P_1/P_s)/dh$, decreases considerably as h increases. Variations of A_2/A_1 as a function of h for both Reference and the revised circuit is shown in Figure A-7. Figure A-8 shows the excursion from the nominal $A_2/A_1 = 0.7$ for the $h = h_N \pm d_{2_R}/10$.

Alternatively, one may consider not operating at the nominal $A_2/A_1 = 0.7$, but rather meeting the constraints of maximum flapper excursion. Figure A-9 shows the value of d_1, d_2, and d_s for that case.

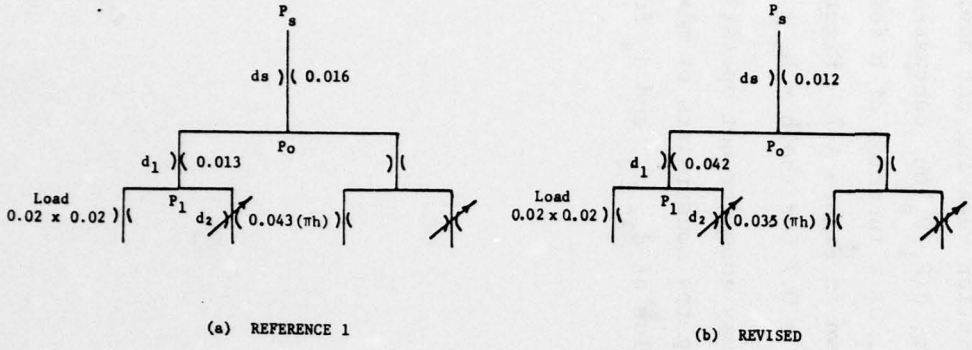

Figure A-5. Resistance bridge diameters for reference 1 and revised bridge circuits

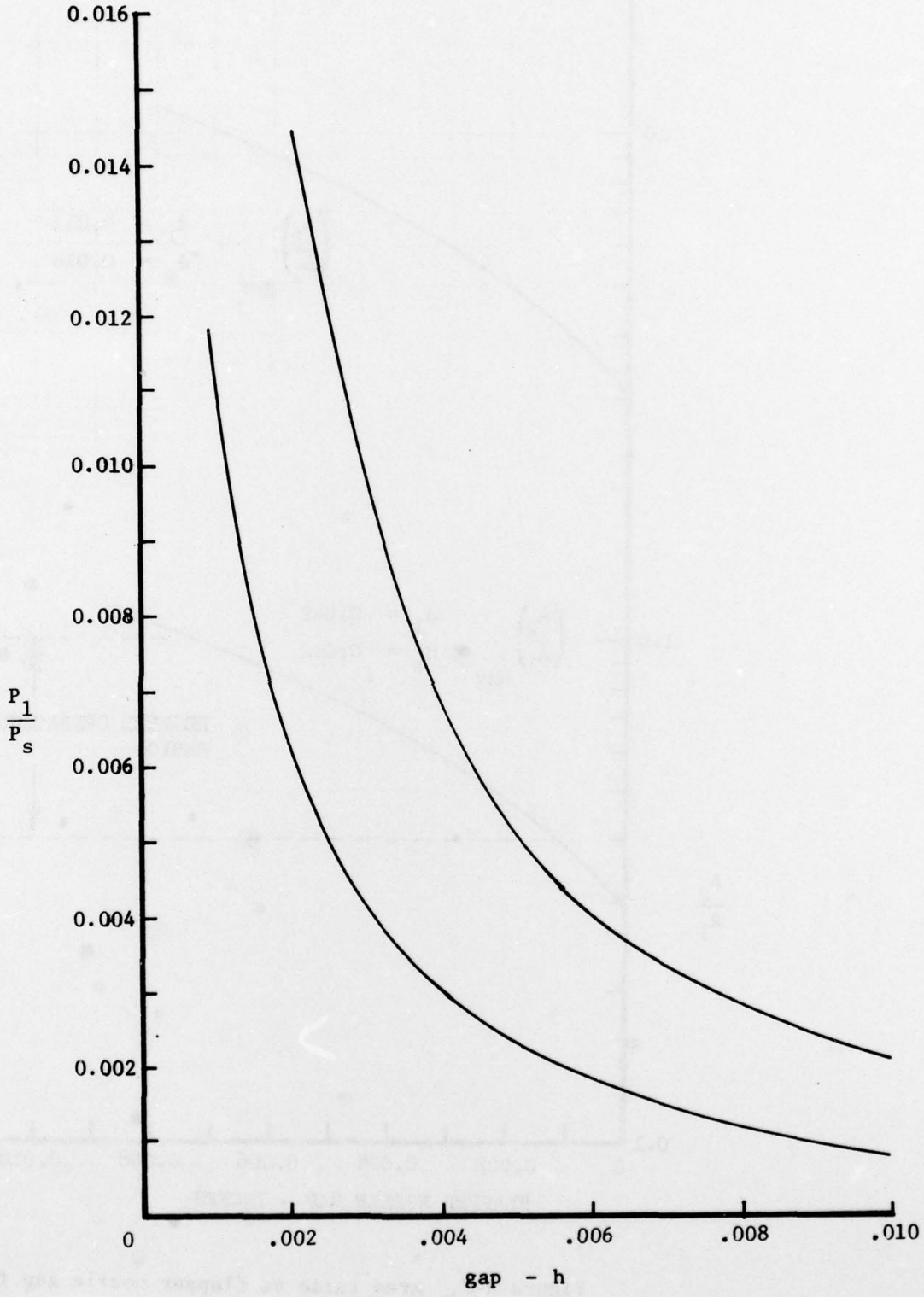

Figure A-6. Flapper nozzle pressure ratio as a function of nozzle gap

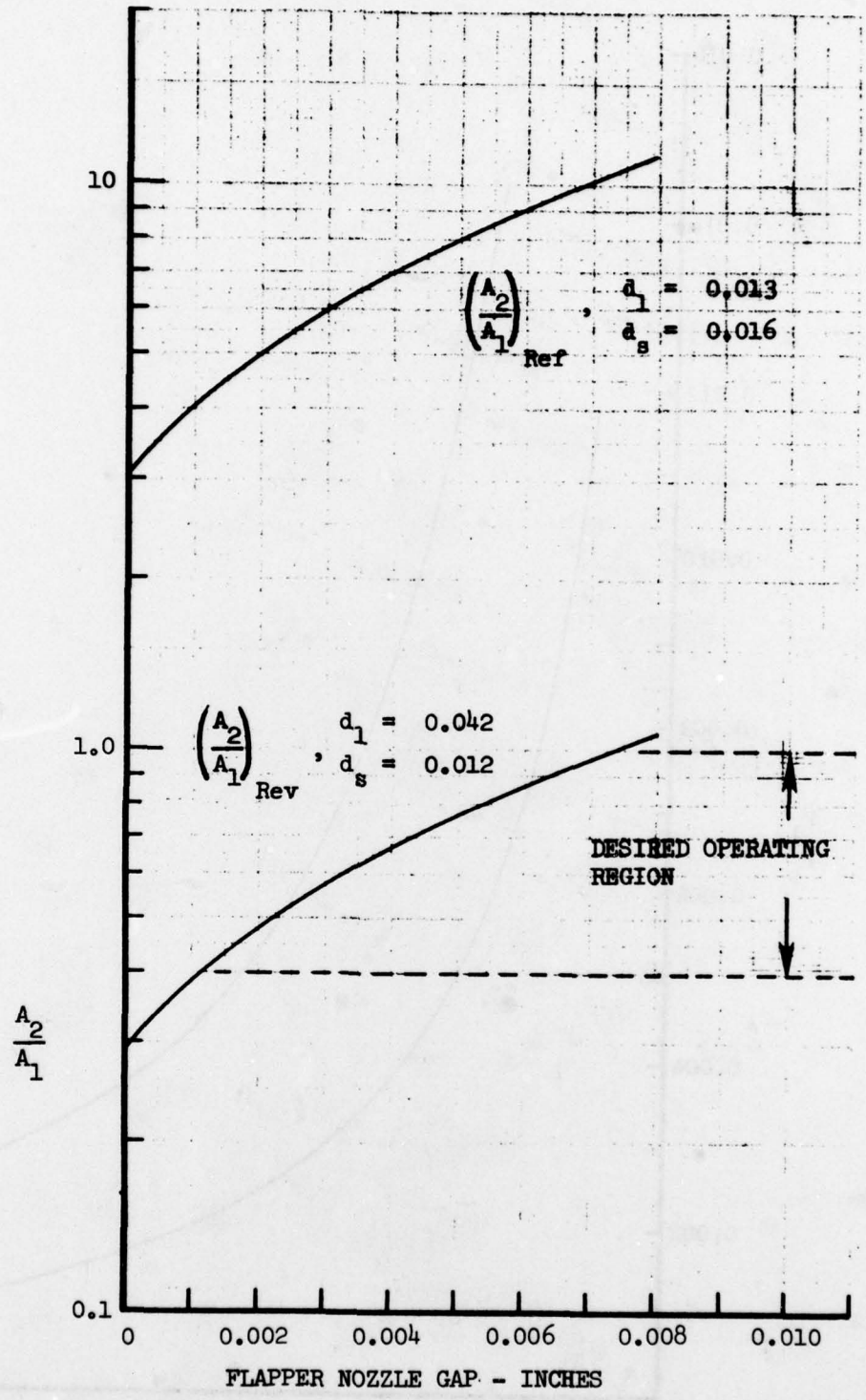

Figure A-7. Area ratio vs flapper nozzle gap for $h_N = \frac{d_2}{10}$ and $d_2 = 0.043$

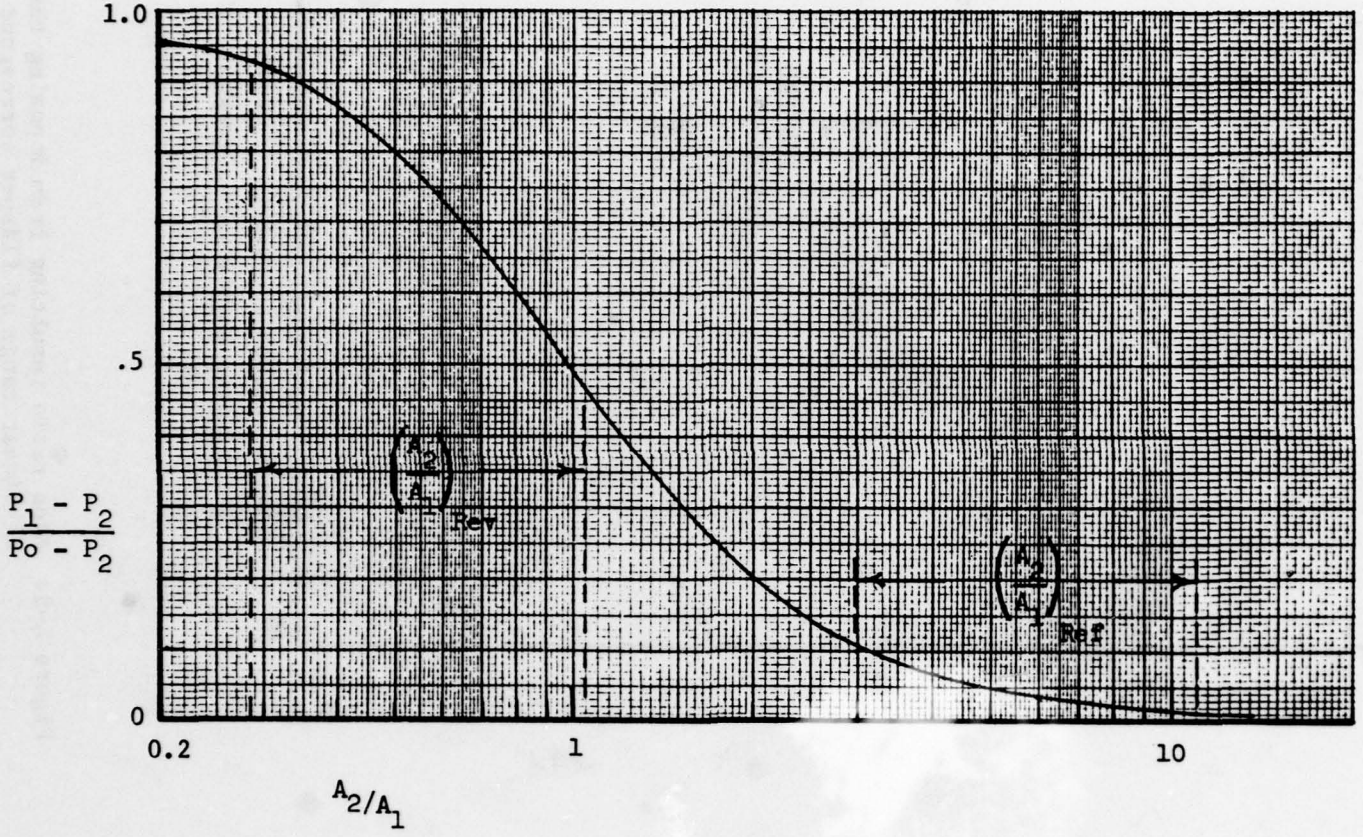

Figure A-8. Comparison of revised area ratio with area ratio of reference 1

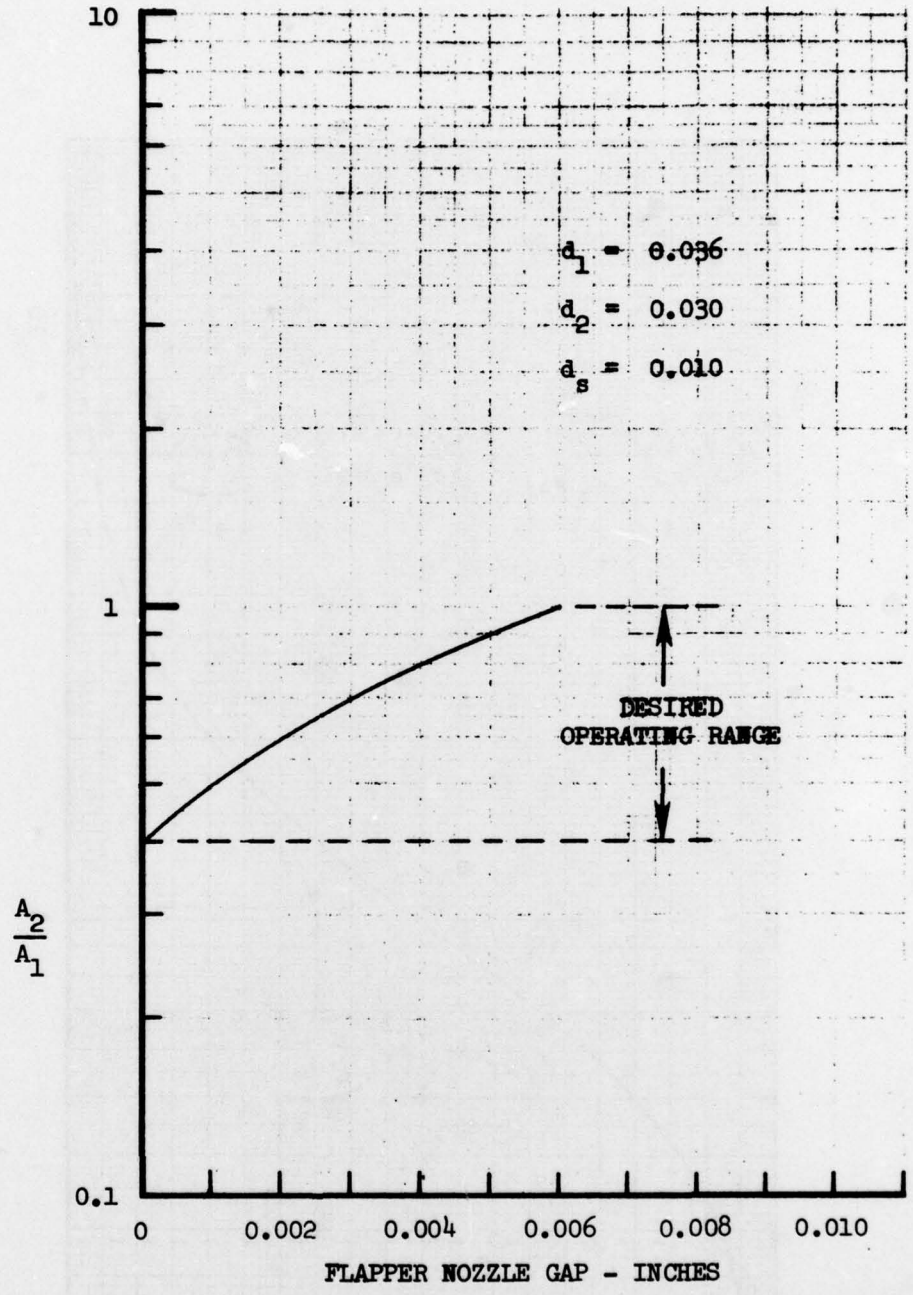

Figure A-9. Area ratio resulting from imposing that ends of linear range of flapper correspond to limits for pure orifice behavior of flapper nozzle

CONCLUSIONS

Under the assumptions regarding gap width and maintaining supply pressure the same as was used in the tests, it appears that the Fluidisc gain can be increased considerably.

DISTRIBUTION

COMMANDER
US ARMY MATERIEL DEVELOPMENT &
READINESS COMMAND
5001 EISENHOWER AVENUE
ALEXANDRIA, VA 22333
ATTN DRXAM-TL, HQ TECH LIBRARY

DIRECTOR
US ARMY BALLISTIC RESEARCH LABORATORY
ABERDEEN PROVING GROUND, MD 21005
ATTN DRDAR-TSB-S (STINFO)

DEFENSE DOCUMENTATION CENTER
CAMERON STATION, BUILDING 5
ALEXANDRIA, VA 22314
ATTN DDC-TCA 12 COPIES

COMMANDER
USA RSCH & STD GP (EUR)
BOX 65
FPO NEW YORK 09510
ATTN LTC JAMES M. KENNEDY, JR.
CHIEF, PHYSICS & MATH BRANCH

DIRECTOR
US ARMY MATERIEL SYSTEMS ANALYSIS
ACTIVITY
ATTN DRXSY-MP
ABERDEEN PROVING GROUND, MD 21005

US ARMY ELECTRONICS RESEARCH
& DEVELOPMENT COMMAND
ATTN WISEMAN, ROBERT S., DR., DRDEL-CT

COMMANDER
USA MISSILE RES & DEV COMMAND
REDSTONE ARSENAL, AL 35809
ATTN DRDMI-TGC, J. C. DUNAWAY
ATTN DRCPM-TOE, FRED J. CHEPLEN

COMMANDER
US ARMY ARRADCOM
DOVER, NJ 07801
ATTN DRDAR-LCN-F, A.E. SCHMIDLIN
ATTN DRDAR-LCW-E, MR. J. CONNORS

COMMANDER
US ARMY MISSILE & MUNITIONS CENTER
& SCHOOL
REDSTONE ARSENAL, AL 35809
ATTN ATSK-CTD-F

COMMANDER
NAVAL AIR DEVELOPMENT CENTER
WARMINSTER, PA 18974
ATTN R. MCGIBONEY, 30424

NAVAL AIR SYSTEMS COMMAND
DEPARTMENT OF THE NAVY
WASHINGTON, DC 20360
ATTN CODE AIR-52022A, J. BURNS
ATTN CODE AIR-52022E, D. HOUCK

COMMANDER
PACIFIC MISSILE RANGE
NAVAL MISSILE CENTER
POINT MUGU, CA 93042
ATTN CODE 3123, ABE J. GARRETT
ATTN CODE 1243, A. ANDERSON

COMMANDER
NAVAL SHIP ENGINEERING CENTER
PHILADELPHIA DIVISION
PHILADELPHIA, PA 19112
ATTN CODE 6772, D. KEYSER

COMMANDER
NAVAL SURFACE WEAPONS CENTER
WHITE OAK, MD 20910
ATTN CODE WA-33, J. O'STEEN

COMMANDER
NAVAL ORDNANCE STATION
INDIANHEAD, MD 20640
ATTN CODE 5123B, J. MORRIS

NAVAL SHIP RES & DEV CENTER
CODE 1619, MR. K. READER
BETHESDA, MD 20084

DISTRIBUTION (Cont'd)

COMMANDER
USA TANK AUTOMOTIVES RES & DEV COMMAND
ARMOR & COMP DIV. DRDTA-RKT
BLDG. 215
WARREN, MI 48090
ATTN M. STEELE

NAVAL SEA SYSTEMS COMMAND
SEA0331H
WASHINGTON, DC 20362
ATTN A. CHAIKIN

COMMANDER
NAVAL WEAPONS CENTER
CHINA LAKE, CA 93555
ATTN CODE 5536, MR. M. D. JACOBSON

COMMANDER
AF AERO PROPULSION LABORATORY, AFSC
WRIGHT-PATTERSON AFB, OH 45433
ATTN LESTER SMALL 1TBC

COMMANDER
AIR FORCE AVIONICS LABORATORY
WRIGHT-PATTERSON AFB, OH 45433
ATTN RWN-2, RICHARD JACOBS

AF INSTITUTE OF TECHNOLOGY, AU
WRIGHT-PATTERSON AFB, OH 45433
ATTN AFIT (ENM), MILTON E. FRANKE

COMMANDER
USA MOBILITY EQUIPMENT R&D CENTER
FORT BELVOIR, VA 22060
ATTN DRDME-EM, R.N. WARE

NASA LANGLEY RESEARCH
HAMPTON, VA 23665
ATTN MS 494, H. D. GARNER
ATTN MS 494, R. R. HELLBAUM

FRANKLIN INSTITUTE OF THE STATE
OF PENNSYLVANIA
20TH STREET & PARKWAY
PHILADELPHIA, PA 19103
ATTN C. A. BELSTERLING

MASSACHUSETTS INSTITUTE OF
TECHNOLOGY
77 MASSACHUSETTS AVENUE
CAMBRIDGE, MA 02139
ATTN DAVID WORMLEY, MECH ENGR DEPT,
RM 3-146

THE UNIVERSITY OF TEXAS AT ARLINGTON
MECHANICAL ENGINEERING DEPARTMENT
ARLINGTON, TX 76019
ATTN DR. ROBERT L. WOODS

AIRESEARCH
P.O. BOX 5217
402 SOUTH 36th STREET
PHOENIX, AZ 85034
ATTN DAVID SCHAFFER
ATTN TREVOR SUTTON
ATTN D. MILLET

CORNING GLASS WORKS
FLUIDIC PRODUCTS
HOUGHTON PARK, B-2
CORNING, NY 14830
ATTN MR. W. SCHEMERHORN

HONEYWELL, INC.
1625 ZARTHAN AVE
MINNEAPOLIC, MI 55413
ATTN J. HEDEEN

US ARMY RESEARCH OFFICE
P.O. BOX 12211
RESEARCH TRIANGLE PARK, NC 27709
ATTN JAMES J. MURRAY, ENG SCI DIV

DIRECTOR
APPLIED TECHNOLOGY LABORATORY
FORT EUSTIS, VA 23604
ATTN GEORGE W. FOSDICK,
DAVDL-EU-SYA

DISTRIBUTION (Cont'd)

HARRY DIAMOND LABORATORIES
ATTN 00100, COMMANDER/TECHNICAL DIR/TSO
ATTN CHIEF, 00210
ATTN CHIEF, DIV 10000
ATTN CHIEF, DIV 20000
ATTN CHIEF, DIV 30000
ATTN CHIEF, DIV 40000
ATTN CHIEF, LAB 11000
ATTN CHIEF, LAB 13000
ATTN CHIEF, LAB 15000
ATTN CHIEF, LAB 22000
ATTN CHIEF, LAB 21000
ATTN CHIEF, 34000
ATTN CHIEF, 36000
ATTN CHIEF, 47000
ATTN CHIEF, 48000
ATTN RECORD COPY, 94100
ATTN HDL LIBRARY, 41000 (5 copies)
ATTN HDL LIBRARY, 41000 (WOODBRIDGE)
ATTN CHAIRMAN, EDITORIAL COMMITTEE
ATTN TECHNICAL REPORTS BRANCH, 41300
ATTN LEGAL OFFICE, 97000
ATTN LANHAM, C., 00210
ATTN WILLIS, B., 47400
ATTN JOYCE, J., 13400 (15 copies)

LIST OF REFERENCES

1. Design Of A Fluidic Missile Control System, Bowles Engineering Corporation, Report R-5-20-66, 1966.

2. Mentzer, William, R. "Pure Fluid Torpedo Control," Bowles Fluidic Corporation, Report No. R-7-18-68.

3. Young, R. "Feasibility Investigation Of A Laminar Angular Rate Sensor (LARS)," prepared under Contract No. N0018-72-C-0231, 1973.

4. Neradka, V. F., "Development of Computer Models For Fluidic Control Systems," TRITEC, INC. Report No. 7001, prepared under Contract No. DAAG39-77-M-3900, 1977.

5. Burton, R. V., "Two Axis Vortex Rate Sensor Package," prepared by Honeywell, Inc. under Contract No. DAAG39-73-C-0159, 1974.

6. Ostdiek, A., "Viscous Vortex Rate Sensor," HDL-TR-1555, 1971.

7. Manion, F. M., Personal Communication, 1978.

8. Manion, F. M., and Drzewiecki, T. M., "Analytical Design of Laminar Proportional Amplifier," Volume I, Fluidic State Of The Art Symposium, October 1974, page 149.